

# Sedimentary pyrite sulfur isotope compositions preserve signatures of the surface microbial mat environment in sediments underlying low-oxygen cyanobacterial mats

Maya L. Gomes<sup>1</sup>  | Judith M. Klatt<sup>2,3</sup>  | Gregory J. Dick<sup>3</sup>  | Sharon L. Grim<sup>3,4</sup> | Kathryn I. Rico<sup>3,5</sup>  | Matthew Medina<sup>3</sup> | Wiebke Ziebis<sup>6</sup> | Lauren Kinsman-Costello<sup>7</sup>  | Nathan D. Sheldon<sup>3</sup>  | David A. Fike<sup>8</sup> 

<sup>1</sup>Department of Earth and Planetary Sciences, Johns Hopkins University, Baltimore, MD, USA

<sup>2</sup>Microsensor Group, Max Planck Institute for Marine Microbiology, Bremen, Germany

<sup>3</sup>Department of Earth and Environmental Science, University of Michigan, Ann Arbor, MI, USA

<sup>4</sup>Exobiology Branch, National Aeronautics and Space Administration Ames Research Center, Mountain View, CA, USA

<sup>5</sup>Department of Earth and Planetary Sciences, McGill University, Montreal, QC, Canada

<sup>6</sup>Department of Biological Sciences, University of Southern California, Los Angeles, CA, USA

<sup>7</sup>Department of Biological Sciences, Kent State University, Kent, OH, USA

<sup>8</sup>Department of Earth and Planetary Sciences, Washington University, Saint Louis, MO, USA

## Correspondence

Maya L. Gomes, Department of Earth and Planetary Sciences, Johns Hopkins University, 3400 N. Charles Street, Baltimore, MD 21218, USA.

Email: mgomes@jhu.edu

## Funding information

Washington University in St. Louis; National Science Foundation

## Abstract

The sedimentary pyrite sulfur isotope ( $\delta^{34}\text{S}$ ) record is an archive of ancient microbial sulfur cycling and environmental conditions. Interpretations of pyrite  $\delta^{34}\text{S}$  signatures in sediments deposited in microbial mat ecosystems are based on studies of modern microbial mat porewater sulfide  $\delta^{34}\text{S}$  geochemistry. Pyrite  $\delta^{34}\text{S}$  values often capture  $\delta^{34}\text{S}$  signatures of porewater sulfide at the location of pyrite formation. However, microbial mats are dynamic environments in which biogeochemical cycling shifts vertically on diurnal cycles. Therefore, there is a need to study how the location of pyrite formation impacts pyrite  $\delta^{34}\text{S}$  patterns in these dynamic systems. Here, we present diurnal porewater sulfide  $\delta^{34}\text{S}$  trends and  $\delta^{34}\text{S}$  values of pyrite and iron monosulfides from Middle Island Sinkhole, Lake Huron. The sediment–water interface of this sinkhole hosts a low-oxygen cyanobacterial mat ecosystem, which serves as a useful location to explore preservation of sedimentary pyrite  $\delta^{34}\text{S}$  signatures in early Earth environments. Porewater sulfide  $\delta^{34}\text{S}$  values vary by up to  $\sim 25\text{‰}$  throughout the day due to light-driven changes in surface microbial community activity that propagate downwards, affecting porewater geochemistry as deep as 7.5 cm in the sediment. Progressive consumption of the sulfate reservoir drives  $\delta^{34}\text{S}$  variability, instead of variations in average cell-specific sulfate reduction rates and/or sulfide oxidation at different depths in the sediment. The  $\delta^{34}\text{S}$  values of pyrite are similar to porewater sulfide  $\delta^{34}\text{S}$  values near the mat surface. We suggest that oxidative sulfur cycling and other microbial activity promote pyrite formation in and immediately adjacent to the microbial mat and that iron geochemistry limits further pyrite formation with depth in the sediment. These results imply that primary  $\delta^{34}\text{S}$  signatures of pyrite deposited in organic-rich, iron-poor microbial mat environments capture information about microbial sulfur cycling and environmental conditions at the mat surface and are only minimally affected by deeper sedimentary processes during early diagenesis.

This is an open access article under the terms of the Creative Commons Attribution-NonCommercial License, which permits use, distribution and reproduction in any medium, provided the original work is properly cited and is not used for commercial purposes.

© 2021 The Authors. *Geobiology* published by John Wiley & Sons Ltd.

## KEY WORDS

geomicrobiology, microbial mats, middle island sinkhole, pyrite, sulfur isotopes

## 1 | INTRODUCTION

Sulfur isotope ( $\delta^{34}\text{S}$ ) signatures of sedimentary pyrite deposited in Precambrian microbial mat environments have been used to investigate microbial sulfur cycling and environmental conditions during the early evolution of life (Fischer et al., 2014; Gomes et al., 2018; Meyer et al., 2017; Wacey et al., 2010). Geological evidence suggests that coastal environments and possibly also the terrestrial realm were shaped by abundant microbial mats throughout Precambrian until the Neoproterozoic, which marks the decline of "matworld" and is linked with the appearance of complex eukaryotic life (Grotzinger & Knoll, 1999; Lenton & Daines, 2017; Peters et al., 2017; Riding, 2006; Walter, 1976). Microbial mat environments are multi-layered ecosystems composed of diverse microbial consortia, which host various types of photosynthetic, chemosynthetic, respiration, and fermentation reactions that drive rapid elemental cycling and shape geochemical gradients within the layers of the mat and the surrounding environment. Precambrian microbial mats likely represented hot spots for the evolution of new avenues of life due to steep physico-chemical gradients and were oases for intense local cycling of compounds that might have not undergone intense redox dynamics on a global scale, such as of sulfur (Des Marais, 2003). Microbial sulfate reduction (MSR) is among the most ancient metabolisms as inferred from isotope signatures, despite a much later onset of abundant sulfate supply to the oceans by weathering after the Great Oxidation Event (Fike et al., 2015; Lyons et al., 2009). Sulfur isotopes can record information about MSR, oxidative sulfur cycling, and environmental conditions and are thus particularly useful for investigating the history of biogeochemical cycling and how microbial mat ecosystems shaped Earth's redox evolution.

Pyrite  $\delta^{34}\text{S}$  signatures in sediments deposited in microbial mat environments are often interpreted based on studies of sulfur isotope patterns in porewater sulfide ( $\delta^{34}\text{S}_{\text{sulfide}}$ ) in modern microbial mats where there is accompanying information about microbial communities and environmental conditions (Fike et al., 2008, 2009; Gomes et al., 2020; Habicht & Canfield, 1997). These studies have shown that depth profiles of  $\delta^{34}\text{S}_{\text{sulfide}}$  values can be explained by differential rates of metabolic activity operating at different depths in the mat, mostly involving microbially mediated sulfate reduction, sulfide oxidation, and sulfur disproportionation processes. The  $\delta^{34}\text{S}_{\text{sulfide}}$  patterns vary over diurnal cycles due to changes in light availability and microbial activity and are also affected by sulfate levels (Fike et al., 2009).

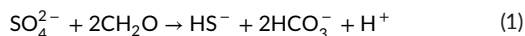
A key question is whether and how  $\delta^{34}\text{S}$  signatures of pyrite ( $\text{FeS}_2$ , often extracted as the operationally defined chromium-reducible sulfide or CRS pool; Canfield et al., 1986) in microbial mats capture  $\delta^{34}\text{S}_{\text{sulfide}}$  variability over diurnal cycles. In marine

settings,  $\delta^{34}\text{S}$  values of pyrite often reflect  $\delta^{34}\text{S}_{\text{sulfide}}$  values at the location(s) of pyrite formation (Lyons, 1997). While it has been shown that pyrite  $\delta^{34}\text{S}$  values are similar to porewater sulfide  $\delta^{34}\text{S}$  values in sediments underlying a cyanobacterial mat (Habicht & Canfield, 1997), the microbial mats that have been the subject of previous studies of diurnal trends in porewater  $\delta^{34}\text{S}$  values lacked significant pyrite formation due to low reactive iron availability (Huerta-Diaz et al., 2011). This hinders our ability to determine how diurnal changes in sulfur cycling and the location(s) of pyrite formation in mats impact  $\delta^{34}\text{S}$  signatures in pyrite deposited in microbial mat ecosystems.

Here, we report  $\delta^{34}\text{S}$  values of porewater sulfide and sequentially extracted sedimentary sulfide mineral phases, including the acid-volatile sulfide fraction (primarily iron monosulfides; Luther, 2005; Rickard & Morse, 2005) and the CRS fraction that is operationally defined as sedimentary pyrite but may also include elemental sulfur (Canfield et al., 1986), in low-oxygen microbial mats in Middle Island Sinkhole (MIS), Lake Huron, USA. Low-oxygen conditions are a result of the combined influence of dense, oxygen-poor groundwater that enters through an alcove at the edge of the sinkhole and sinks to cover the mat-water interface and low rates of oxygen production via oxygenic photosynthesis (Biddanda et al., 2006; Ruberg et al., 2008; Biddanda and Weinke, accepted). In addition to being a useful site for studying geochemical records of sulfur cycling because pyrite is present in the sediments (Rico & Sheldon, 2019), MIS is also a valuable early Earth analog because it hosts low-oxygen cyanobacterial mats that were likely to be common in ancient, low-oxygen oceans (Dick et al., 2018; Grotzinger & Knoll, 1999). We show that  $\delta^{34}\text{S}_{\text{sulfide}}$  patterns can be explained by progressive consumption of the sulfate reservoir. Diurnal changes in  $\delta^{34}\text{S}_{\text{sulfide}}$  patterns are driven by changes in net sulfate reduction at different depths in the sediment underlying the mat, which vary in response to light-driven changes in microbial communities and other taxa that affect porewater chemistry as deep as 7.5 cm within the sediment. Despite dynamic  $\delta^{34}\text{S}_{\text{sulfide}}$  gradients, pyrite  $\delta^{34}\text{S}$  values do not change significantly with depth and are similar to  $\delta^{34}\text{S}_{\text{sulfide}}$  values recorded at the mat surface. These results, combined with previously published iron geochemistry data (Rico & Sheldon, 2019), indicate that pyrite primarily forms near the mat-water interface and captures  $\delta^{34}\text{S}_{\text{sulfide}}$  signatures in the upper portions of the microbial mat. Surface microbial communities are likely to play a major role in promoting pyrite formation at the surface, and iron geochemistry (Rico & Sheldon, 2019) limits pyrite formation in deeper portions of the sediment. These results have implications for the interpretation of pyrite sulfur isotope records preserved in sediments deposited in ancient microbial mat environments.

## 1.1 | Sedimentary sulfur isotope geochemistry

Sulfur isotope signatures in sedimentary pyrite record information about ancient sulfur cycling (Canfield & Farquhar, 2009; Fike et al., 2015). Sulfur isotopes are expressed in delta notation as permil (‰) deviations from an international standard ( $\delta^{34}\text{S} = \{[(^{34}\text{S}/^{32}\text{S}_{\text{sample}})/(^{34}\text{S}/^{32}\text{S}_{\text{standard}})]-1\} \times 1000$ ; where the standard is the Vienna Canyon Diablo Troilite or V-CDT). The dominant process that fractionates sulfur isotopes is MSR, where microorganisms use sulfate ( $\text{SO}_4^{2-}$ ) to oxidize organic matter ("CH<sub>2</sub>O"), producing bisulfide (H<sub>2</sub>S), bicarbonate (HCO<sub>3</sub><sup>-</sup>), and a hydrogen ion (H<sup>+</sup>):



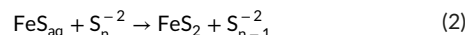
Sulfur isotope fractionation between sulfate and sulfide ( $\epsilon_{\text{MSR}} = \delta^{34}\text{S}_{\text{sulfide}} - \delta^{34}\text{S}_{\text{sulfate}}$ ) during MSR can be up to 70‰ and is commonly negatively correlated with cell-specific sulfate reduction rate (Harrison & Thode, 1958; Canfield et al., 2010; Sim et al., 2011; Leavitt et al., 2013). Thus, strain-specific relationships between cell-specific sulfate reduction rates and environmental conditions such as sulfate concentrations, mechanisms of sulfate transport across the cell membrane, organic carbon type and availability, and nutrient limitation and co-limitation impact  $\delta^{34}\text{S}$  values of sulfate and sulfide (Bradley et al., 2016). Reservoir effects can also impact  $\delta^{34}\text{S}$  values of sulfate and sulfide when sulfate levels are low and/or MSR is active in locations with limited system openness (Gomes & Hurtgen, 2013, 2015; Jorgensen, 1979; Pasquier et al., 2017). The reservoir effect can be modeled as an irreversible reaction with a kinetic isotope effect occurring in a closed system (i.e., Rayleigh fractionation; Mariotti et al., 1981) where the isotopic composition of the product approaches the isotopic composition of the initial reactant reservoir as the reactant reservoir is progressively consumed. Oxidative sulfur cycling reactions can also fractionate sulfur isotopes. However, magnitudes of these fractionations are generally low (~7 to 5‰; see compilations in Zerkle et al., 2009; Gomes and Johnston, 2017; or Pellerin et al., 2019) compared with MSR, although fractionations of as low as ~18‰ or as high as 18‰ have been reported at low pH (Kaplan & Rittenberg, 1964; Nakai & Jensen, 1964; Taylor et al., 1984) and for disproportionation reactions (Bottcher et al., 2001) or sulfide oxidation under alkaline conditions (Pellerin et al., 2019), respectively.

Sulfur isotope values of pyrite ( $\delta^{34}\text{S}_{\text{pyrite}}$ ) capture isotopic signatures of ambient sulfide at the location of pyrite formation (e.g., at different locations in the sediment column or in the water column versus the sediment; Lyons, 1997), and therefore, recorded values are not always representative of an entire system where they form. For example, it has been shown that  $\delta^{34}\text{S}_{\text{pyrite}}$  values can differ from porewater sulfide  $\delta^{34}\text{S}$  values by up to ~30‰, likely due to pyrite precipitation in biofilms utilizing sulfide that is the immediate product of sulfate reduction (Raven et al., 2016). Thus, information about both porewater sulfide and pyrite  $\delta^{34}\text{S}$  patterns in modern microbial mats is particularly valuable for investigating what paleoenvironmental

information is recorded in  $\delta^{34}\text{S}_{\text{pyrite}}$  signatures in sediments deposited in microbial mat environments.

## 1.2 | Pyrite formation

Relating the effects of microbial activity and environmental conditions on porewater  $\delta^{34}\text{S}$  values to the pyrite  $\delta^{34}\text{S}$  record requires accounting for the timing and location of pyrite formation and differentiating microbial impacts from post-depositional overprinting. Pyrite formation in natural systems is thought to occur through either the polysulfide ( $\text{S}_n^{2-}$ ) pathway (eqn. 2, the Bunsen reaction) or the hydrogen sulfide (H<sub>2</sub>S) pathway (eqn. 3, the Berzelius reaction or Wächtershauser reaction; Rickard & Luther, 2007; Rickard, 2012):



where FeS is iron monosulfide, which forms from the reaction of H<sub>2</sub>S and Fe(II) in locations where pyrite formation is favorable (Rickard & Luther, 2007). Pyrite is the stable iron sulfide phase in Earth surface environments (Rickard, 2012; Rickard & Luther, 2007). However, pyrite formation is limited by the kinetic inhibition of pyrite nucleation, which requires supersaturated solutions (Rickard, 2012; Rickard & Luther, 2007; Schoonen & Barnes, 1991).

The mechanism that limits pyrite nucleation and therefore formation differs between the two pathways. For the polysulfide pathway (eqn. 2), high polysulfide concentrations increase rates of pyrite formation, and thus, the reaction between polysulfide and an iron species is the rate-controlling step (Rickard, 1975). For the hydrogen sulfide pathway (eqn. 3), the rate-controlling step is the electron transfer between S(-II) and H(I) via an inner sphere complex between FeS and H<sub>2</sub>S (Rickard & Luther, 1997; Rickard, 1997). More broadly, it is thought that microbes can play a role in promoting pyrite formation—via direct effects on precipitation (Thiel et al., 2019) or due to templating on cell walls or other organic substrates (Donald & Southam, 1999; Rickard et al., 2007). Conversely, some types of organic matter can hinder pyrite formation (e.g., aldehydic carbonyls; Rickard et al., 2001). These studies provide insights into why pyrite formation often occurs near the transition to sulfidic waters in modern systems; for example, sedimentary pyrite in the Black Sea captures the  $\delta^{34}\text{S}$  signature of sulfide at the top of the zone of sulfate reduction, which occurs in the water column, rather than deeper in the water column and/or sediment (Lyons, 1997). Reactants involved in the rate-limiting steps (i.e.,  $\text{S}_n^{2-}$ , H<sub>2</sub>S, and  $\text{FeS}_{\text{aq}}$ ) are stable and/or formed by microbial activity in these locations, resulting in supersaturated conditions that promote pyrite nucleation and formation (Rickard, 2012; Rickard & Luther, 2007). These steep geochemical gradients occur in microbial mats and shift over diurnal cycles (e.g., Fike et al., 2008, 2009). Thus, knowledge of how these gradients shape  $\delta^{34}\text{S}_{\text{pyrite}}$  signatures will improve our ability to use the

geological record to investigate the coupled evolution of life and the Earth surface.

## 2 | METHODS

### 2.1 | Study site

A modern analog for Proterozoic cyanobacterial mats with pyrite formation can be found in Middle Island Sinkhole (MIS), MI, USA (45°11.914 N, 83°19.671°W; Figure 1). MIS is a submerged depression in Lake Huron formed by the collapse of Devonian aged carbonates of the Traverse group. The ~10,000 m<sup>2</sup> depression lies ~13 m below the surrounding lake floor at a water depth of 23 m (Biddanda et al., 2006; Ruberg et al., 2008) and is overlain by high-conductivity water (specific conductivity of ~2300  $\mu$ s/cm) that emerges from a seep (termed the alcove) located in the south-east edge of the sinkhole (Biddanda et al., 2006; Ruberg et al., 2008). The ionic strength of the water arises from dissolution of salts due to reactions between groundwater and limestones and evaporites from the Middle Devonian Detroit River Group that underlies the Traverse group (Biddanda et al., 2006; Ruberg et al., 2008). Density stratification inhibits mixing with the overlying water, resulting in low-oxygen (~2–4 mg/L) waters overlying the sediment–water interface (SWI; Ruberg et al., 2008). Light penetration to the SWI supports a dynamic microbial mat ecosystem (Biddanda et al., 2006, 2015; Grim, 2019; Kinsman-Costello et al., 2017; Nold et al., 2010; Snider et al., 2017; Voorhies et al., 2012, 2016).

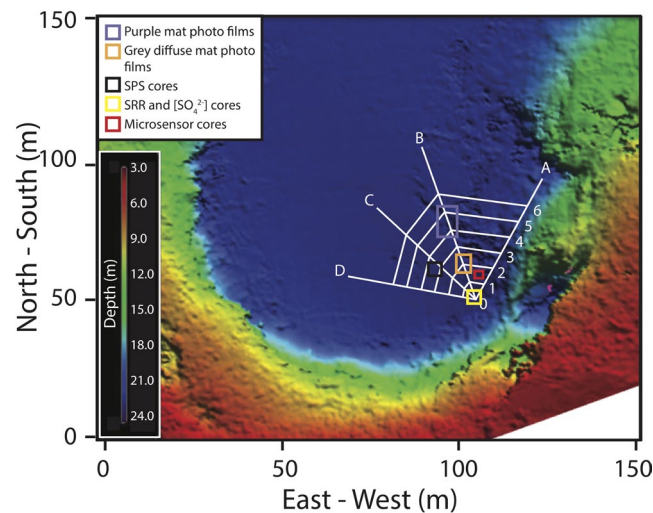


**FIGURE 1** Bathymetric image of Middle Island Sinkhole (from Nold et al., 2013) with sampling grid in white and showing locations of purple mat photographic film deployments (purple box), gray mat photographic film deployments (orange box), core for solid-phase sulfide (SPS) sediment geochemistry (black box), cores for sulfate reduction rate (SRR) and porewater sulfate concentration ( $[\text{SO}_4^{2-}]$ ) determination (yellow box), and cores for ex situ microsensor measurements (red box).

Much of the SWI of the flat, deep portion of the sinkhole is covered with ~2-mm-thick purple mats dominated by cyanobacterial groups taxonomically similar to *Phormidium* and *Planktothrix* (Nold et al., 2010; Voorhies et al., 2012, 2016). Patches of white, filamentous sulfide-oxidizing bacteria, such as *Beggiatoa* or *Epsilonproteobacteria*, are also variably present at the SWI (Biddanda et al., 2006, 2015; Nold et al., 2010; Voorhies et al., 2012). Both the purple cyanobacteria and the white filamentous bacteria are capable of vertical migration, and therefore, the surface appearance of the mat can change over diurnal cycles (Biddanda et al., 2015; Nold et al., 2010; Voorhies et al., 2012). Deltaproteobacteria, including various potential sulfate reducers, are abundant within the mat and underlying sediment (Kinsman-Costello et al., 2017). Eukaryotic taxa identified in the mats by 18S rRNA gene surveys include ciliates, nematodes, and tardigrades (Nold et al., 2010). Microscopy confirmed the presence of many of these eukaryotic taxa, as well as diatoms (Merz et al., 2020).

Sediment underlying the ~2 mm-thick microbial mats is different than the surrounding Lake Huron sediment (Nold et al., 2013; Rico & Sheldon, 2019; Rico et al., 2020). Carbon isotope signatures in the sedimentary organic matter underlying the mats indicate that it is sourced from settling phytoplankton (Nold et al., 2013; Rico & Sheldon, 2019; Rico et al., 2020), and some trace metals such as molybdenum show modest enrichments due to particulate shuttling (Rico et al., 2019). Overall, the MIS sediments have higher total organic carbon, iron, and trace metal concentrations than Lake Huron sediments due to differences in redox chemistry and geomicrobiological conditions between the sinkhole and surrounding environment (Nold et al., 2013; Rico & Sheldon, 2019; Rico et al., 2019, 2020).

### 2.2 | Sampling

Sampling, *in situ* deployments, site characterization, and site photography were carried out by SCUBA divers from The Thunder Bay National Marine Sanctuary Dive Unit. Sediment cores were hand-collected using plexiglass tubes that were inserted into the sediment and then sealed with rubber stoppers before extraction. The cores were used to assess (1) sulfate reduction rates and porewater sulfate concentrations; (2) porewater sulfide, pH, and dissolved oxygen dynamics using microsensors under controlled laboratory conditions; and (3) sulfur isotope compositions of solid-phase sulfides. *In situ* deployments of black and white photographic film were used to capture diurnal  $\delta^{34}\text{S}_{\text{sulfide}}$  patterns in the porewater (Fike et al., 2017). Water emerging from the alcove was sampled by a peristaltic pump for (1) analysis of sulfate  $\delta^{34}\text{S}$  values and (2) use in ex situ microsensor measurements. *In situ* deployments, water sampling for sulfate  $\delta^{34}\text{S}$  analysis, core collection for sulfate reduction rate, and porewater sulfate concentration measurements were performed over the course of a 2-week field campaign in July 2016. Cores for solid-phase sulfide sulfur isotope geochemistry were sampled in

Deployment interval	Date	Time in	Time out	Deployment duration (h)
Morning	7/21/2016	9:30	13:30	4
Afternoon	7/23/2016	15:00	17:30	2.5
Evening	7/22/2016	16:30	22:00	5.5
Night	7/22/2016-7/23/2016	22:15	2:45	4.5

**TABLE 1** Deployment times and durations for photographic films used to trap porewater sulfide over a diurnal cycle to determine pore water  $\delta^{34}\text{S}_{\text{sulfide}}$  patterns

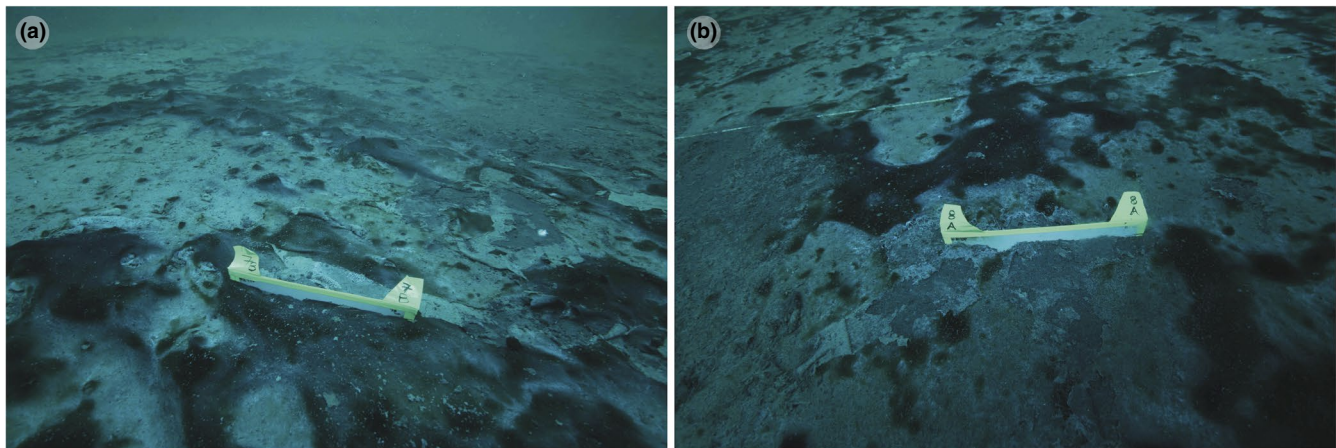


**FIGURE 2** Black and white photographic film deployed in (A) a purple mat location and (B) a gray mat location in the afternoon (15:00–17:30). Film width is 25.4 cm. Deployment times of all films are provided in Table 1.

2015. Cores and water for *ex situ* microsensor measurements were collected in May 2017.

### 2.3 | Sulfate reduction rates and porewater sulfate concentrations

Two sediment cores for porewater sulfate concentration and five sediment cores (ID 2.5 cm) for sulfate reduction rate measurements were obtained from locations covered with purple mat (near node A0 in Figure 1). Cores were transported upright and in the dark back to land, where incubations were done the same day that the cores were collected.

Sulfate reduction rates were measured according to the whole-core injection method (Jørgensen, 1978). Radio-labeled sulfate (200 kBq  $^{35}\text{SO}_4$  dissolved in 6  $\mu\text{l}$  water) was injected in 1-cm depth intervals. After injection, cores were incubated in a water bath at *in situ* temperature ( $\sim 9^\circ\text{C}$ ) in the dark for 20 min. After incubation, cores were sectioned at 1-cm intervals. Sulfate reduction was stopped by transferring core sections immediately into 10 ml of ice-cold 20% zinc acetate. Sulfate reduction rates were determined using the cold chromium distillation for radiolabeled sulfide (Fossing & Jørgensen, 1989; Kallmeyer et al., 2004).

Porewater from a separate set of two cores was obtained by centrifugation of 1-cm sediment sections and subsequent filtration of the supernatant with 0.45- $\mu\text{m}$  PES syringe filters. Samples were flash frozen in liquid butane and kept frozen until analysis. Sulfate concentration in the porewater was determined by membrane-suppression

ion chromatography (Dionex, Thermo Scientific). Uncertainty of sulfate concentration analyses is  $<2\%$ , determined as the relative standard deviation of check standards.

### 2.4 | Ex situ microsensor measurements

Cores (ID 10 cm) with purple mat and water taken between nodes A1, A2, B1, and B2 in Figure 1 were transported to the laboratory in Ann Arbor, MI upright, in the dark, and cooled. During measurements, the core was kept at  $14^\circ\text{C}$  and the water column was covered with paraffin oil to prevent exchange with air. The water column was fed with MIS bottom water using a peristaltic pump from a thermostated recycling reservoir to adjust a gentle flow across the mat–water interface and purged with  $\text{N}_2$ –air mixtures to adjust oxygen concentration. Light was supplied from a halogen light source (Schott). Light intensity was assessed with a cosine-corrected quantum sensor connected to a light meter (both LI-COR).

Microsensors for dissolved oxygen ( $\text{O}_2$ ),  $\text{H}_2\text{S}$ , and pH determination were built, calibrated and used as described previously (de Beer et al., 1997; Jeroschewski et al., 1996; Revsbech, 1989). Uncertainty of these measurements is  $\pm 12\%$  for  $\text{O}_2$ ,  $\pm 3\%$  for  $\text{H}_2\text{S}$ , and  $\pm 0.1\%$  for pH. Total sulfide concentrations ( $\Sigma[\text{S}^{2-}]$ ,  $[\text{HS}^-]$ ,  $[\text{H}_2\text{S}]$ , where brackets denote concentration) were calculated from the  $\text{H}_2\text{S}$  and pH profiles using a  $\text{pK}_a$  of 7.16. Profiles were measured under different light and dissolved oxygen levels to examine whether dynamics in pH,  $\text{O}_2$ , and sulfide concentration could be explained by the presence of cable bacteria (e.g. Nielsen et al., 2010; Pfeffer et al., 2012; Seitaj et al.,

2015). Conditions were as follows: (1) light (58  $\mu\text{mol photons/m}^2/\text{s}$ ) to mimic mid-day light conditions at MIS (cf., Merz et al., 2020) and ~130  $\mu\text{M O}_2$  and (2) dark (<0.5  $\mu\text{mol photons/m}^2/\text{s}$ ) and ~13  $\mu\text{M O}_2$  in the overlying water column. Profiles under both conditions (light and dark, low  $\text{O}_2$ ) were measured in the same spot over the course of ~1 h – time scales that are sufficiently long to differentiate the impact of cable bacteria versus diffusion on chemical profiles (e.g., Nielsen et al., 2010), but sufficiently short that processes related to cm-scale migration of diatoms and other diurnally varying processes should not affect pH,  $\text{O}_2$ , and sulfide trends (Merz et al., 2020).

## 2.5 | Deployments for porewater sulfide sulfur isotope geochemistry

Black and white photographic film (Ilford Delta 100 Professional) was used to capture 2D patterns of porewater sulfide sulfur isotope geochemistry by reaction between porewater sulfide and silver within the film, forming silver sulfide (Fike et al., 2017). Over a period of three days (July 21–23, 2016), the films were deployed for 2.5–5.5 h at four time intervals to explore changes in porewater sulfide  $\delta^{34}\text{S}$  values over diurnal cycles (Table 1): morning (9:30–13:30), afternoon (15:00–17:30), evening (16:30–22:00), and night (22:15–2:45). The films were deployed at locations (Figure 1) with two different surface characteristics: (1) sediment covered with purple microbial mat during the day and white mat at night, hereafter termed the purple mat (located near nodes B4 and B5 in Figure 1; image of a deployed film shown in Figure 2a) and (2) gray sediment lacking visible cohesive mat at the surface with white material variably present (located near node B2 in Figure 1; image of a deployed film shown in Figure 2b), hereafter termed the gray mat. In total, 8 films were deployed (i.e., four time intervals at two sites). Pictures of deployed films were taken at the beginning and end of each deployment. After retrieval, films were removed from sunlight, rinsed, and allowed to dry before storage in the dark. Images of deployed films and appearance after removal, rinsing, and drying are shown in Figures S1–S8.

Sulfide was extracted from film sections cut at 1-cm intervals by boiling in 6N hydrochloric acid for 2 h in an anoxic reaction vessel. The hydrogen sulfide gas released by the reaction was driven via a  $\text{N}_2$  carrier gas through a citric acid and sodium citrate-buffered water trap ( $\text{pH} = 4$ ) into a trap vessel with 1 M silver nitrate to precipitate the sulfide as silver sulfide. The silver sulfide was purified by rinsing with 1 M ammonium hydroxide solution and rinsed three times with deionized water. Sulfide yields from films were determined gravimetrically.

Silver sulfide samples were mixed with vanadium pentoxide and combusted to  $\text{SO}_2$  for sulfur isotope analysis on a Costech Elemental Analyzer coupled to a DeltaV Isotope ratio mass spectrometer at Washington University. S isotope measurements were reproducible within 0.2‰ based on repeat analysis of international standards (IAEA S1 and IAEA S3) and the Washington University in-house  $\text{Ag}_2\text{S}$ ,  $\text{BaSO}_4$ , and  $\text{ZnS}$  standards. All porewater sulfide  $\delta^{34}\text{S}$  data

were corrected to account for the small ( $1.2 \pm 0.5\text{‰}$ ) known offset between aqueous sulfide and sulfide trapped in photographic films associated with sulfide diffusion into the film and the reaction with silver to form  $\text{Ag}_2\text{S}$  (Fike et al., 2017).

## 2.6 | Solid-phase sulfide sulfur isotope geochemistry

Two sediment cores were used for solid-phase sulfide  $\delta^{34}\text{S}$  analysis (location near node C3 in Figure 1). No specific mat types were targeted for core extraction because the appearance of mats at the sediment–water interface varies from year to year and sediment geochemistry is time-averaged. Sediment geochemistry was preserved by placing the cores on dry ice; cores were transported frozen to the University of Michigan in Ann Arbor, MI, where they were stored at  $-20^\circ\text{C}$ . Frozen cores were sectioned via table saw according to depth (three 1-cm sections at the top, then 3 cm downcore). Sections were freeze-dried and homogenized prior to analysis.

A sequential procedure was used to extract operationally defined pools of sedimentary sulfide: (1) acid-volatile sulfide (AVS), which is predominantly iron monosulfides (Chanton & Martens, 1985), and (2) chromium-reducible sulfide (CRS), which recovers pyrite and elemental sulfur (Canfield et al., 1986). Sediment was placed in reaction vessels, which were purged of oxygen using  $\text{N}_2$  gas. The AVS was first extracted by boiling in 6N HCl for 2 h (Chanton & Martens, 1985), and the CRS was then extracted by boiling the residual sediment with acidified chromium (II) chloride solution for 2 h (Canfield et al., 1986). For both AVS and CRS extractions, the liberated hydrogen sulfide was driven via a  $\text{N}_2$  carrier gas through a citric acid and sodium citrate-buffered water ( $\text{pH} = 4$ ) into the silver nitrate solution filled trap vessel to trap the sulfide as silver sulfide. The silver sulfide was purified, rinsed, and analyzed for  $\delta^{34}\text{S}$  values as previously described in section 2.5.

The sequential extraction procedure was done on samples that had been previously freeze-dried, homogenized, and stored under ambient atmospheric conditions. It is likely that some components of the AVS pool may have been lost during sample handling; nonetheless, the sequential extraction procedure was performed in order to preclude mixing of the CRS and AVS pools. It is unlikely that the storage conditions impacted sulfur isotope signatures of CRS because fractionations associated with abiotic oxidation of pyrite in the presence of oxygen are low (<1‰; Balci et al., 2007).

## 2.7 | Sulfate sulfur isotope geochemistry

Alcove water samples were treated with 3% zinc acetate solution in the field to trap any sulfide as zinc sulfide. After transport back to the laboratory, the samples were filtered at 0.45  $\mu\text{m}$  to remove zinc sulfide and any other particulates. Saturated barium chloride solution was added to the filtered samples to precipitate sulfate as barium sulfate. Purification of the barium sulfate was done using

the diethylenetriaminepentaacetic acid dissolution and reprecipitation procedure (D-DARP; Bao, 2006). Barium sulfate samples were mixed with vanadium pentoxide, and  $\delta^{34}\text{S}$  values were determined as described in Section 2.3.

### 3 | RESULTS

#### 3.1 | Site conditions

In July 2016, much of the sediment–water interface (SWI) of the Middle Island Sinkhole (MIS) was dominated with surface coverings that were similar to those described in previous studies (Biddanda et al., 2006, 2015; Kinsman-Costello et al., 2017; Nold et al., 2010, 2013; Ruberg et al., 2008; Snider et al., 2017; Voorhies et al., 2012): purple mats, gray sediment lacking cohesive mat, and intermittently observed white patches. We chose to focus on the two most commonly observed surface coverings to study diurnal  $\delta^{34}\text{S}$  patterns in porewater sulfide in 2016: the purple mats and gray sediment with diffuse mat at the SWI (i.e., gray mats) as two common end-member environments (Figure 2). The thickness of the purple mat was ~2 mm. The diffuse gray mat lacked a substantial cohesive mat layer at the surface (Figure 2).

#### 3.2 | Sulfate reduction rates and porewater sulfate concentrations

Sulfate reduction rates in the sediment underlying the purple mat (Figure 3; Table S1) are highest just below the SWI at 0.5 cm (mean = 1803.7 nmol/cm<sup>3</sup>/day,  $\sigma$  = 896.8 nmol/cm<sup>3</sup>/day;  $n$  = 5) and decrease to low and variable values deeper in the sediment (between ~25 and ~835 nmol/cm<sup>3</sup>/day, with one potential outlier value of 1707.7 nmol/cm<sup>3</sup>/day at 5.5 cm). There is a second peak in sulfate reduction rates at 5.5 cm, consistent with the concave shape

of the concentration depth profiles (Figure 3). The mean sulfate reduction rate at this depth was 841.6 nmol/cm<sup>3</sup>/day ( $\sigma$  = 502.6 nmol/cm<sup>3</sup>/day;  $n$  = 5) or 625.1 nmol/cm<sup>3</sup>/day ( $\sigma$  = 156.0 nmol/cm<sup>3</sup>/day;  $n$  = 4) if the potential outlier is removed. However, given that the increase in sulfate reduction rate is not defined by one point and is reproducible in all five cores, it is not likely to be an analytical artifact and therefore may be representative of the natural variability in the system. Sulfate concentrations decreased from  $5.3 \pm 0.2$  mM at 0.5 cm to  $0.1 \pm 0.03$  mM at 9.5 cm (Figure 3; Table S1). There was a slight increase in sulfate concentrations to  $0.6 \pm 0.5$  mM at 10.5 cm before sulfate concentrations continue to decrease to  $0.5 \pm 0.6$  mM at 11.5 cm (although this deep sulfate concentration variability was only observed in one porewater profile).

#### 3.3 | Ex situ microsensor measurements of O<sub>2</sub>, pH, and sulfide

Ex situ microsensor measurements were done on purple mat and underlying sediments under illumination mimicking mid-day light conditions at MIS (58  $\mu\text{mol}$  photons/m<sup>2</sup>/s; Merz et al., 2020; Biddanda and Weinke, accepted). Concentrations of O<sub>2</sub> were ~125  $\mu\text{M}$  in the overlying water, peaked at 271.4  $\mu\text{M}$  at 0.5 mm in the mat, decreased to undetectable levels by 2 mm, and remained undetectable in the sediment underlying the mat (Figure 4; Table S2). Sulfide was undetectable in the mat and started to increase at 2.75 mm, reaching a maximum of 5.1 mM in the deepest measurements (48.5; Figure 4; Table S2). A peak in pH (8.2) occurred at 0.5 mm in the mat overlapping with the O<sub>2</sub> peak, consistent with photosynthetic O<sub>2</sub> production (e.g., Revsbech et al., 1983). The pH peak was followed by a rapid decline to 7.3 at 1.25 mm in the zone of O<sub>2</sub> and sulfide consumption, suggesting aerobic sulfide oxidation to sulfate (Klatt & Polerecky, 2015). Below the mat, pH gradually increased to ~7.7 in the deepest measurements (48.5 mm; Figure 4; Table S2). Upon darkening and adjustment of water column O<sub>2</sub> concentrations to ~13  $\mu\text{M}$ , the

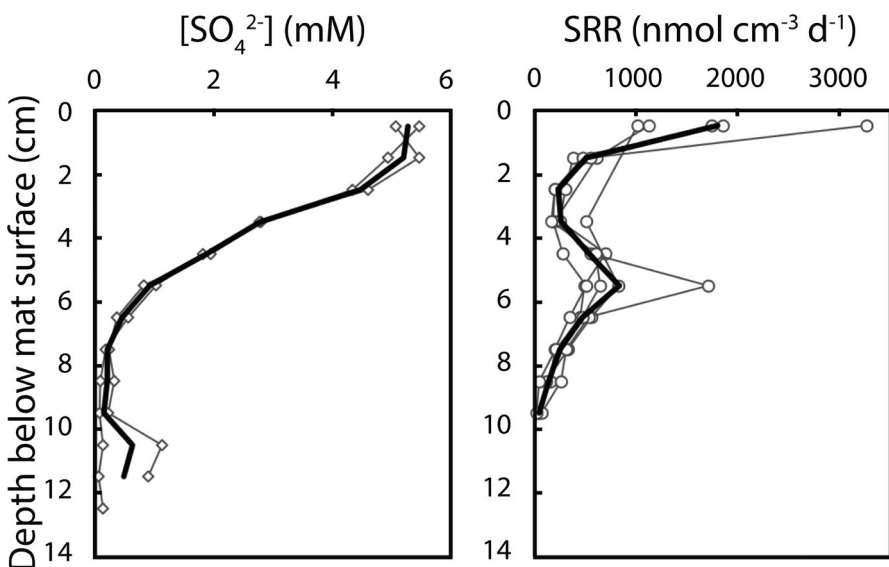


**FIGURE 3** Porewater sulfate concentration ( $[\text{SO}_4^{2-}]$ ; left) and sulfate reduction rates (SRR; right) from dark incubations. Gray symbols show the results of individual analyses with analytical errors smaller than the size of the symbol. The solid black line is the average of all analyses. Data are provided in Table S1.

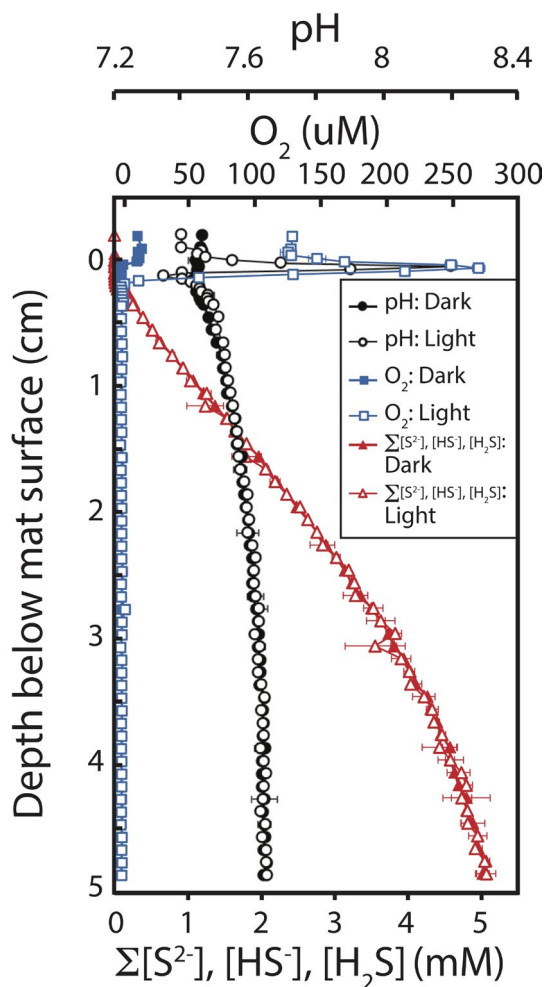


**FIGURE 4** Profiles of pH (black circles),  $O_2$  concentrations (blue squares), and total sulfide concentrations ( $\Sigma[S^{2-}]$ ,  $[HS^-]$ ,  $[H_2S]$ , where brackets denote concentration; red triangles) from *ex situ* microsensor measurements under light (58  $\mu\text{mol}$  photons/ $\text{m}^2/\text{s}$ ; open symbols) and dark, low  $O_2$  ( $<0.5 \mu\text{mol}$  photons/ $\text{m}^2/\text{s}$  and  $\sim 13 \mu\text{M}$   $O_2$ ; closed symbols) conditions measured within  $\sim 1$  h in the same location in a core with a surface purple mat. Data are provided in Table S2.

photosynthetic  $O_2$  concentration and pH peak disappeared and the zone of aerobic sulfide oxidation moved to the uppermost 0.5 mm. Changes in the light regime and  $O_2$  concentration in the water column over  $\sim 30$  min to 1 h did not affect the concentration profiles beyond the uppermost 3 mm.

### 3.4 | Sulfur isotope patterns

Porewater sulfide was recovered using photographic film (Fike et al., 2017) from all analyzed depth intervals at all times of day except for the uppermost sample (0.5 cm) from the purple mat in the afternoon. All of the porewater sulfide sulfur isotope ( $\delta^{34}\text{S}_{\text{sulfide}}$ ) profiles show similar patterns (Figure 5; Table S3);  $\delta^{34}\text{S}_{\text{sulfide}}$  values were low ( $-7.1\text{--}11.1\text{\textperthousand}$ ) near the SWI relative to deeper portions of the

mat, where  $\delta^{34}\text{S}_{\text{sulfide}}$  values stabilized at  $\sim 15\text{--}18\text{\textperthousand}$  with maximum values reached at  $\sim 1\text{--}8$  cm below the mat surface (Figure 5; Table S3). The deep  $\delta^{34}\text{S}_{\text{sulfide}}$  values ( $\sim 15\text{--}18\text{\textperthousand}$ ) were slightly lower than  $\delta^{34}\text{S}_{\text{sulfate}}$  in the alcove water, which had an average  $\delta^{34}\text{S}$  value of  $18.9\text{\textperthousand}$  ( $\sigma = 0.16\text{\textperthousand}$ ;  $n = 4$ ).

The magnitude of surface porewater sulfide  $^{34}\text{S}$  depletion and the depth where  $\delta^{34}\text{S}_{\text{sulfide}}$  values approach  $\delta^{34}\text{S}_{\text{sulfate}}$  values varied with time of day and between the purple and gray mats. In the purple mat, night and morning  $\delta^{34}\text{S}_{\text{sulfide}}$  patterns were similar (Figure 5; Table S3). In the afternoon, sulfide levels were too low at 0.5 cm to measure  $\delta^{34}\text{S}_{\text{sulfide}}$  values. The depth where  $\delta^{34}\text{S}_{\text{sulfide}}$  values approached their maximum also gets lower in the afternoon reaching  $\sim 15\text{\textperthousand}$  only at 7.5 cm. In the evening, the  $\delta^{34}\text{S}_{\text{sulfide}}$  profile was  $^{34}\text{S}$ -enriched compared with other times in the day, with a  $\delta^{34}\text{S}_{\text{sulfide}}$  value of  $11.1\text{\textperthousand}$  at 0.5 cm and approaching maximum values at 1.5 cm. In the gray diffuse mat,  $\delta^{34}\text{S}_{\text{sulfide}}$  values were generally higher at the surface compared with purple mat and the depth at which values reach their maximum was less dynamic. Maximum values were approached at 4.5 cm in the evening, night, and morning (Figure 5; Table S3). In the evening,  $\delta^{34}\text{S}_{\text{sulfide}}$  values in the surface were slightly enriched compared with night and morning ( $3.5\text{\textperthousand}$  vs  $\sim 2\text{\textperthousand}$ ). In the afternoon, the  $\delta^{34}\text{S}_{\text{sulfide}}$  profiles were the most  $^{34}\text{S}$ -enriched, with a  $\delta^{34}\text{S}_{\text{sulfide}}$  value of  $11.0\text{\textperthousand}$  below the SWI (0.5 cm) increasing to high values ( $\sim 15\text{--}16\text{\textperthousand}$ ) at 1.5 cm.

Sequentially extracted sedimentary sulfides include the operationally defined pools of acid-volatile sulfide (AVS; primarily composed of iron monosulfides) and chromium-reducible sulfide (CRS; primarily composed of pyrite and elemental sulfur). Due to sample drying prior to the sequential extraction procedure and storage at ambient atmospheric conditions, it is likely that some component of the AVS was lost. In many of the samples, especially deep ( $>10.5$  cm) samples, there was insufficient recovery of AVS for  $\delta^{34}\text{S}_{\text{AVS}}$  analyses.

Similar to the  $\delta^{34}\text{S}_{\text{sulfide}}$  patterns,  $\delta^{34}\text{S}_{\text{AVS}}$  values were lowest near the SWI and became  $^{34}\text{S}$ -enriched with depth (Figure 6; Table S4). In the October core,  $\delta^{34}\text{S}_{\text{AVS}}$  values were  $-0.3\text{\textperthousand}$  at the surface, increased to  $9.9\text{\textperthousand}$  at 2.5 cm, and then decreased slightly to  $7.8\text{\textperthousand}$  at 10.5 cm. In the July core,  $\delta^{34}\text{S}_{\text{AVS}}$  values ranged between  $-7.3\text{\textperthousand}$  and  $-3.4\text{\textperthousand}$  in the top 3 cm and then became higher but also quite variable, reaching a value of  $18.5\text{\textperthousand}$  at 7.5 cm before decreasing to  $5.7\text{\textperthousand}$  at 10.5 cm. CRS showed the smallest amount of  $^{34}\text{S}$  variability;  $\delta^{34}\text{S}_{\text{CRS}}$  values ranged from  $\sim 10$  to  $1\text{\textperthousand}$  in both the July and October 2015 cores. There was a slight pattern of  $^{34}\text{S}$  enrichment with depth in both cores, but  $\delta^{34}\text{S}_{\text{CRS}}$  values never reached the high  $^{34}\text{S}$  values in porewater sulfide ( $\sim 15\text{--}18\text{\textperthousand}$ ) measured from deeper sediments ( $>5$  cm below SWI).

## 4 | DISCUSSION

### 4.1 | Diurnal trends in porewater sulfide

Profiles in both purple and gray mats at Middle Island Sinkhole (MIS) show similar trends of low porewater  $\delta^{34}\text{S}_{\text{sulfide}}$  values ( $-7.1\text{--}11.1\text{\textperthousand}$ ) at the sediment-water interface (SWI) that increase with

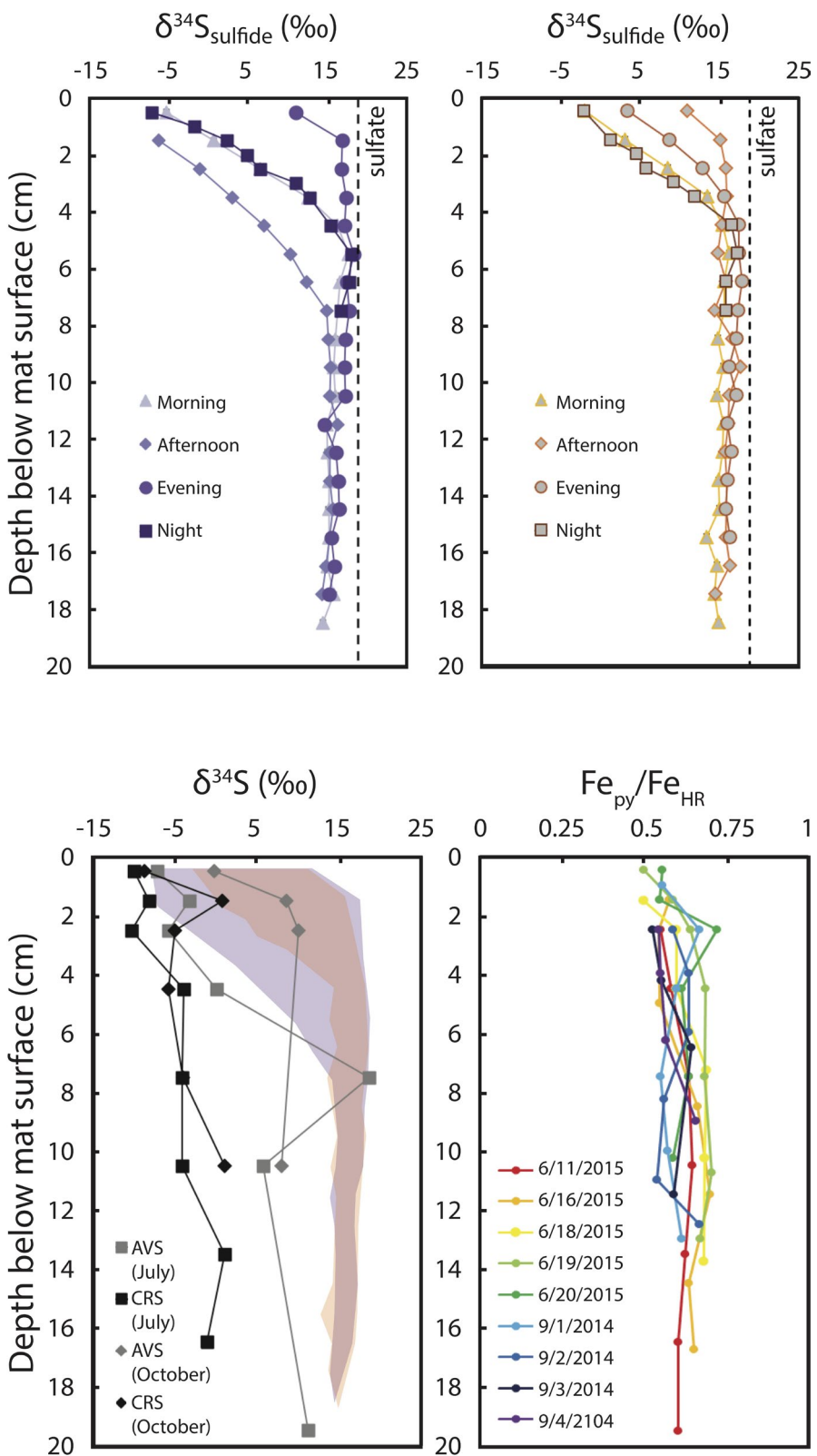


**FIGURE 5** Porewater sulfide sulfur isotope ( $\delta^{34}\text{S}_{\text{sulfide}}$ ) values from purple (left) and diffuse gray (right) mat locations. The sulfur isotope composition of sulfate ( $\delta^{34}\text{S}_{\text{sulfate}}$ ) in water emerging from the alcove is indicated on both plots with a dashed line. Reproducibility of S isotope measurements is 0.2‰ (i.e., within the size of the symbols) based on standard deviation of international standard analyses. Deployment times are provided in Table 1. Data are provided in Table S3.

**FIGURE 6** Solid-phase sulfur and iron geochemistry. Left: Sulfur isotope composition ( $\delta^{34}\text{S}$ ) of acid-volatile sulfide (AVS; squares) and chromium-reducible sulfide (CRS; diamonds) from cores taken in July 2015 (gray) and October 2015 (black). The range of  $\delta^{34}\text{S}_{\text{sulfide}}$  values in porewater from the purple and gray diffuse mat locations is shown in shaded purple and orange, respectively. Reproducibility of S isotope measurements is 0.2‰ (i.e., within the size of the symbols) based on standard deviation of international standard analyses. Data are provided in Table S4. Right: Concentration of Fe as pyrite (wt %) from nine cores taken in 2014 and 2015 from data published in Rico and Sheldon (2019).

depth as the sulfate reservoir is progressively consumed (Figures 3 and 5). Consumption of the sulfate reservoir by MSR is consistent with previously measured porewater sulfate and sulfide concentration profiles (Kinsman-Costello et al., 2017). These concentration

and isotope patterns are often attributed to Rayleigh isotope fractionation under closed system conditions (e.g., Jorgensen, 1979). In order to determine whether the  $\delta^{34}\text{S}_{\text{sulfide}}$  trends are due to progressive consumption of the sulfate reservoir (i.e., Rayleigh isotope

fractionation or the reservoir effect), we use an approximation of the isotopic evolution of the product of an irreversible reaction in closed system (after Mariotti et al., 1981):

$$\delta^{34}S_{H2S,d} = -\frac{\epsilon(1-f)\ln(1-f)}{f} + \delta^{34}S_{SO4,0} \quad (4)$$

where  $\delta^{34}S_{H2S,d}$  is the sulfur isotope composition of sulfide at depth  $d$ ,  $\epsilon$  is the average apparent sulfur isotope fractionation effect ( $^{34}\epsilon_{MSR}$ ),  $f$  is the fraction of sulfate remaining at depth  $d$ , and  $\delta^{34}S_{SO4,0}$  is the sulfur isotope composition of sulfate when  $f = 0$ . This approximation linearizes the relationship between the fraction of sulfate remaining and  $\delta^{34}S_{H2S}$  value at each depth such that the slope of the line is the average apparent sulfur isotope fractionation that is likely dominated by sulfate reduction ( $^{34}\epsilon_{MSR}$ ) and the y-intercept is the S isotope composition of the sulfate reservoir ( $\delta^{34}S_{SO4,0}$ ; Mariotti et al., 1981; Mandernack et al., 2003). We used the porewater  $\delta^{34}S_{\text{sulfide}}$  data from the afternoon purple mat profile and sulfate concentration data from cores sampled in the purple mat in the afternoon as inputs into the equation. These data fit a linear regression ( $r^2 = 0.95, n = 12$ ) where the slope of the line is  $-22.7\text{\textperthousand}$  and the y-intercept is  $18.8\text{\textperthousand}$  (Figure 7). The value for  $^{34}\epsilon_{MSR}$  predicted from this model ( $-22.7\text{\textperthousand}$ ) is within the range of sulfur isotope fractionations during sulfate reduction reported for microbial mats at Solar Lake (Habicht & Canfield, 1997), which had similar sulfate reduction rates to those measured here. Additionally, the  $\delta^{34}S_{SO4,0}$  value ( $18.8\text{\textperthousand}$ ) is similar (i.e., within uncertainty of  $0.2\text{\textperthousand}$ ) to the  $\delta^{34}S$  value of sulfate emanating from the alcove ( $18.9\text{\textperthousand}$ ). Setting the y-intercept to the  $\delta^{34}S$  value of sulfate emanating from the alcove ( $18.9\text{\textperthousand}$ ) yields a similar  $^{34}\epsilon_{MSR}$  value ( $-22.8\text{\textperthousand}$ ) to that predicted by the porewater data alone ( $-22.7\text{\textperthousand}$ ). Thus, the  $\delta^{34}S_{\text{sulfide}}$  data can be explained by progressive consumption of the sulfate reservoir with depth

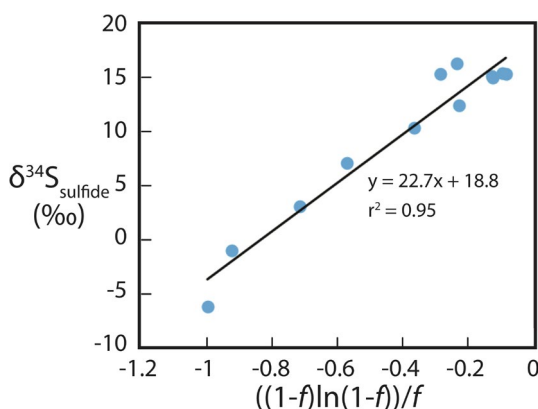


**FIGURE 7** Porewater sulfide sulfur isotope evolution using the Mariotti et al., (1981) approximation of isotopic evolution of a product of a reaction with a kinetic isotope effect in a closed system. The linear regression predicts the average apparent sulfur isotope fractionation effect that is most likely dominated by microbial sulfate reduction ( $^{34}\epsilon_{MSR}$ ) as the slope of the line and the sulfur isotope composition of the initial sulfate reservoir as the y-intercept.

such that deep  $\delta^{34}S_{\text{sulfide}}$  values approach the  $\delta^{34}S$  value of the sulfate reservoir.

Porewater sulfide sulfur isotope ( $\delta^{34}S_{\text{sulfide}}$ ) patterns vary throughout the day in both purple and gray diffuse mats at Middle Island Sinkhole (MIS; Figure 5). Given that  $\delta^{34}S_{\text{sulfide}}$  patterns are driven by progressive consumption of the sulfate reservoir, changes in the  $\delta^{34}S_{\text{sulfide}}$  values throughout the day are caused by variation in net sulfate consumption with depth in the mat and underlying sediment. In particular, when the sulfate reservoir is nearly completely consumed,  $\delta^{34}S_{\text{sulfide}}$  values approach the  $\delta^{34}S$  value of the overlying sulfate reservoir. The depth where  $\delta^{34}S_{\text{sulfide}}$  values reach  $\sim 15\text{--}18\text{\textperthousand}$  moves between 1.5 and 7.5 cm throughout the day. While changes in geochemistry within and immediately adjacent to the  $\sim 2$  mm-thick mat may be driven by light cycles, light only penetrates down to  $\sim 750$   $\mu\text{m}$  within the mat (Merz et al., 2020). Therefore, the deep (up to 7.5 cm below the SWI)  $\delta^{34}S_{\text{sulfide}}$  dynamics are unlikely due directly to diurnal trends in light availability. Instead, we must ask what processes influence variation in rates of sulfate reduction and sulfide oxidation at different depths in the mat and sediment over diurnal cycles. In what follows, we review diurnal changes in the geomicrobiology of the surface mat and then explore potential mechanisms—migration of bacteria, migration of diatoms, sulfide oxidation by cable bacteria—that potentially drive  $\delta^{34}S_{\text{sulfide}}$  trends in the sediment underlying the mat.

The purple mats contain cyanobacteria capable of both anoxicogenic and oxygenic photosynthesis, large sulfide-oxidizing bacteria, and sulfate-reducing bacteria including some with the genetic potential for sulfur disproportionation (Nold et al., 2010; Voorhies et al., 2012, 2016; Klatt et al., 2017; Sharrar et al., 2017; Grim, 2019; Biddanda and Weinke, accepted). Over a diurnal light cycle, activity in the purple mat transitions between predominantly anoxicogenic photosynthesis in the morning until the early afternoon to simultaneous anoxicogenic and oxygenic photosynthesis in the afternoon and evening (Figure 8; Klatt et al., 2017; Biddanda and Weinke, accepted). These diurnal changes are linked with changes in the surface appearance of the mat; the surface of the mat is white in the morning because it is dominated by chemosynthetic sulfide-oxidizing bacteria, becomes purple in the afternoon when purple cyanobacteria are at the surface, and then becomes white again in the late evening and night (Klatt et al., 2017; Biddanda and Weinke, accepted). Anoxicogenic photosynthesis throughout the day is sustained by the sulfide flux from underneath the mat and local sulfide production within the photic zone (Voorhies et al., 2012). This is consistent with the observation that the mat and sediment between 0 and 1 cm depth below the SWI have high rates of sulfate reduction relative to the sediment below ( $1803.7 \text{ nmol} \pm 896.8 \text{ nmol/cm}^3/\text{day}$  at 0.5 cm versus  $\sim 25$  to  $\sim 835 \text{ nmol/cm}^3/\text{day}$  in the deeper sediment; Figure 3; Table S1). The consumption of sulfate by sulfate reduction near the surface may also play a role in limiting diffusion of sulfate to the deeper sediment. The gray mat lacks cohesion at the surface and does not have the purple cyanobacteria that drive changes in rates of gross anoxicogenic and oxygenic photosynthesis throughout the day. The gray mat does contain a diffuse layer of chemosynthetic

## Purple Mat

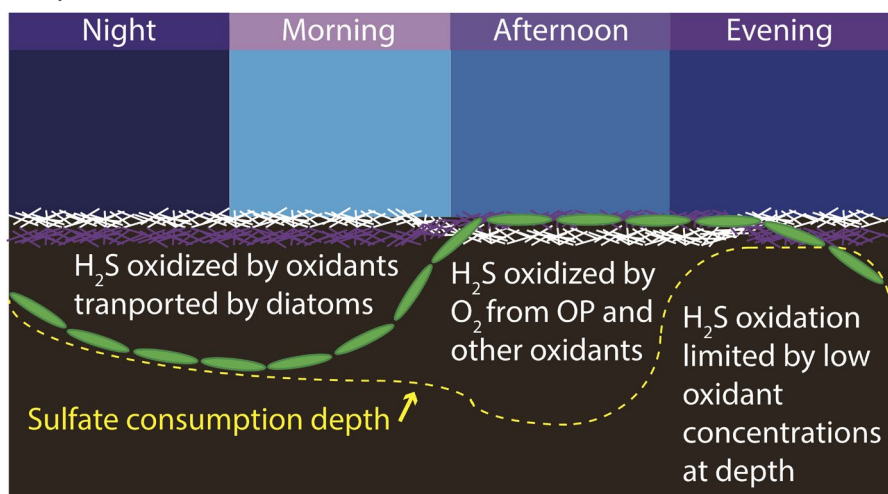
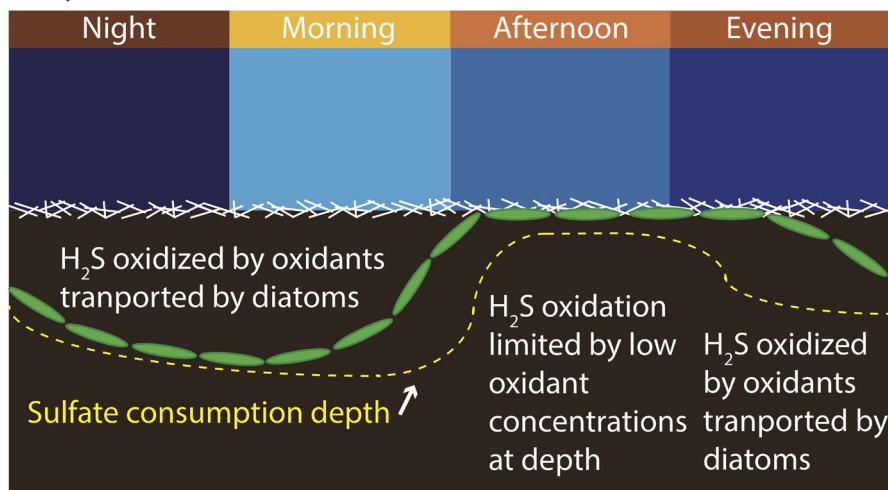


**FIGURE 8** Schematic showing diurnal changes in the depth of near-complete sulfate consumption in sediment underlying purple (top) and gray (bottom) mats. Purple and white lines near the sediment–water interface indicate filamentous purple cyanobacteria and sulfide-oxidizing bacteria, respectively. Green ovals depict migratory diatoms.

## Grey Mat



sulfide-oxidizing bacteria that can play a role in sulfide oxidation at the mat surface (Klatt et al., 2017; Biddanda and Weinke, accepted). Although diurnal changes in geomicrobiological cycling in the surface mat impact net sulfate consumption and  $\delta^{34}\text{S}_{\text{sulfide}}$  values near the SWI, additional processes that vary with depth throughout the day must drive the deeper (>1 cm)  $\delta^{34}\text{S}_{\text{sulfide}}$  trends.

Many bacterial taxa capable of motility have been identified in the MIS mats (Biddanda et al., 2015; Nold et al., 2010; Voorhies et al., 2012). If motile bacteria in the mats are able to migrate to depths >1 cm below the SWI, their activities could play a role in diurnal changes in deep  $\delta^{34}\text{S}_{\text{sulfide}}$  trends. For example, some migratory filamentous sulfide-oxidizing bacteria can reduce intracellular reservoirs of elemental sulfur to sulfide (Schwedt et al., 2012). A diurnal migration over this distance would imply a migration speed of >2  $\mu\text{m/s}$ , which is in the range of previously reported values (e.g., Dunker et al., 2011). However, large vacuolated filamentous sulfur oxidizers similar to the sulfide-oxidizing bacteria with intracellular elemental reservoirs that have been the subject of the migratory studies have not been found at MIS (Kinsman-Costello et al., 2017; Merz et al., 2020; Nold et al., 2010). Thus, although the large sulfide-oxidizing

bacteria at MIS may migrate down and release elemental sulfur or sulfide at depth, it is unlikely that the sulfide-oxidizing mat-forming microbial communities alone shape these patterns. Another option is that the zone of sulfate reduction moves due to migration of sulfate-reducing bacteria. Sulfate-reducing bacteria have been reported to reach a speed of up to 63  $\mu\text{m/s}$  in aqueous solution (Krekeler et al., 1998). As migration over multiple cm has not been observed previously, this would represent an extreme rate of migration of these taxa on a daily basis, with unknown competitive advantage considering the energetic requirements for migration. Thus, it is unlikely that migration of either sulfide-oxidizing or sulfate-reducing bacteria drives the deep  $\delta^{34}\text{S}_{\text{sulfide}}$  trends.

Diatoms are common components of benthic microbial mat ecosystems (Longphuirtet al., 2009; Guarini et al., 2009; Cahoon, 1999; Macintyre et al., 1996) and have been shown to migrate vertically over diurnal cycles (Cartaxana et al., 2008; Pinckney & Zingmark, 1991; Round & Palmer, 1966). Diatoms also are one of the few eukaryotic taxa that are capable of dissimilatory nitrate reduction to ammonium (DNRA) using intracellularly stored nitrate (Kamp et al., 2011). In the MIS mats and sediment, the migration of diatoms is

linked to variations in rates of DNRA (Merz et al., 2020). Isotope labeling indicates that these migrating diatoms take up nitrate near the SWI in the afternoon and then migrate downward where they conduct DNRA. The diatoms reach maximum depths of 4 cm between ~2am and 7am, before returning to the SWI at around noon (Figure 8). This diurnal migration matches diurnal variations in the depth where sulfate is nearly completely consumed (as indicated by the depth where  $\delta^{34}\text{S}_{\text{sulfide}}$  values approach  $\delta^{34}\text{S}$  values of the sulfate reservoir) in the gray mats. Thus, it is possible that oxidants transported by the vertical migration of diatoms directly or indirectly stimulate sulfide oxidation at cm-scale depths in the sediment below the gray mats. While the depth where sulfate is nearly completely consumed below the purple mats is similar to maximum depths that diatoms reach in the morning, evening, and night, either these taxa migrate to greater depths in the afternoon than have been shown previously or additional processes are necessary to explain the sulfur isotope geochemistry of the purple mats in the afternoon.

Cable bacteria are filamentous microorganisms that oxidize hydrogen sulfide by transporting electrons along cm-scale distances in sediment (Nielsen et al., 2010; Pfeffer et al., 2012). Although these sulfide oxidizers are appealing candidates for explaining the deep (>1 cm)  $\delta^{34}\text{S}_{\text{sulfide}}$  trends, none of the 16S rRNA gene data from 0 to 12 cm depths matches with >95% similarity to known cable bacterial 16S rRNA genes (Grim, 2019), indicating that there are no taxa at MIS that are similar at the genus level to known cable bacteria (Kjeldsen et al., 2019). It is possible that taxonomically novel cable bacteria are present at MIS. However, pH profiles (Figure 4) do not display the pH typology associated with sulfide oxidation via cable bacteria and changes in  $\text{O}_2$  concentration in the surface layer and water column did not change sulfide concentrations with depth over ~30-min to 1-h timescales (Nielsen et al., 2010; Pfeffer et al., 2012; Seitaj et al., 2015). The apparent absence of cable bacteria might be due to sediment reworking by diatoms inhibiting their activity (Malkin et al., 2014). Thus, although we cannot rule out that cable bacteria are impacting diurnal  $\delta^{34}\text{S}_{\text{sulfide}}$  trends, we currently lack evidence that these taxa are present at MIS.

We still lack an explanation for why the depth where sulfate is completely consumed increases to 7.5 cm in the afternoon in the sediment underlying the purple mat. The shape of the  $\delta^{34}\text{S}_{\text{sulfide}}$  profile in the afternoon in the purple mat sediment is similar to the night and morning profiles, but shifted 1–2 cm lower. Net oxygen production in the purple mat may result in higher rates of sulfide oxidation near the SWI and play a role in shifting the  $\delta^{34}\text{S}_{\text{sulfide}}$  profile lower. This is consistent with poor sulfide recovery in samples closest to the SWI. Thus, the activity of phototrophic organisms in the surface mat may influence the differences in the depth at which sulfate is nearly completely consumed between the purple and gray mats by impacting other organisms. The migration patterns of the diatoms are shaped by the amount of nitrate captured near the surface and the rate at which they consume it at depth (Merz et al., 2020). Therefore, it is possible that oxidant production by cyanobacteria in the purple mat promotes nitrification and increases the amount of nitrate that diatoms can store, enabling the diatoms to travel to greater depths in

the purple mat than in the gray mat. In sum, although it is likely that the diurnal  $\delta^{34}\text{S}_{\text{sulfide}}$  patterns are determined by the activity of both the surface mat communities and the migrating diatoms (Figure 8), we cannot rule out that other geomicrobiological processes (e.g., motile bacteria or cable bacteria) are also impacting the sulfur cycle over cm scales in the sediment underlying the mat.

## 4.2 | Comparison with other modern microbial mats

Previous work on diurnal trends in sulfur isotope geochemistry of microbial mats was done with mats from Guerrero Negro, Baja California Sur, Mexico (Fike et al., 2009). Guerrero Negro mat  $\delta^{34}\text{S}_{\text{sulfide}}$  patterns were documented at higher spatial resolution (i.e., sub-mm resolution over ~1-cm length scale) than our results from MIS (i.e., cm resolution over ~8–20 cm). Nonetheless, both systems show changes in  $\delta^{34}\text{S}_{\text{sulfide}}$  values over diurnal cycles. Sulfide in Guerrero Negro mats is  $^{34}\text{S}$ -enriched by ~20–25‰ in the top 1–2 mm of the mat relative to the deep portions (Fike et al., 2008, 2009), and there was vertical migration of the  $\delta^{34}\text{S}_{\text{sulfide}}$  pattern over diurnal cycles (Fike et al., 2009). The  $\delta^{34}\text{S}_{\text{sulfide}}$  trends were attributed to differential metabolic activity of S cycling microorganisms throughout the mats; higher rates of sulfate reduction and/or sulfide oxidation at the mat surface result in lower sulfur isotope fractionations between sulfate and sulfide such that  $\delta^{34}\text{S}_{\text{sulfide}}$  values are higher at the surface. Greater light intensity at Guerrero Negro relative to MIS impacts oxidant availability (Canfield & Des Marais, 1993), which may promote sulfide oxidation at Guerrero Negro and thus the differential metabolic effect over the reservoir effect in determining  $\delta^{34}\text{S}_{\text{sulfide}}$  patterns at Guerrero Negro. The striking difference between MIS and Guerrero Negro  $\delta^{34}\text{S}_{\text{sulfide}}$  patterns could be due to the different resolution of measurements, with the cm resolution here masking a potential enrichment at the surface. However, the microbial mats from Little Ambergris Cay, Turks, and Caicos Islands show a similar pattern as Guerrero Negro of  $^{34}\text{S}$ -depleted sulfide near the mat surface over cm scales (Gomes et al., 2020). Although only measured during the daytime, this  $\delta^{34}\text{S}_{\text{sulfide}}$  pattern was attributed to differential metabolic activity, with a potential additional influence of mixing of sulfide with different  $\delta^{34}\text{S}_{\text{sulfide}}$  signatures due to tidal pumping. No  $^{34}\text{S}$  enrichment in sulfide over cm scales was documented in a study of sulfur isotope geochemistry in cyanobacterial mats at Solar Lake, Sanai, Egypt; however, no peak in sulfate reduction rates was documented *in situ* (Habicht & Canfield, 1997). Thus, sulfur isotope geochemistry at MIS is different than these previously studied mat sites because the  $\delta^{34}\text{S}_{\text{sulfide}}$  pattern over cm scales is dominated by progressive consumption of the sulfate reservoir rather than differential metabolic activity, despite sulfate reduction rates being highest at the surface (Figure 5).

A potential explanation for the difference in the shape of  $\delta^{34}\text{S}_{\text{sulfide}}$  profiles between MIS and previously studied mat sites is the difference in sulfate concentration between these systems. The previously studied sites have salinities greater than seawater and

therefore sulfate concentrations greater than seawater concentrations (28mM; Fike et al., 2008, 2009; Habicht & Canfield, 1997; Gomes et al., 2020). Importantly, sulfide production was not sufficient to completely consume the sulfate reservoir at any of these sites (Fike et al., 2008, 2009; Habicht & Canfield, 1997; Present et al., 2018). In contrast, sulfate concentrations in water overlying the mat at MIS are  $\sim 7.1 \pm 1.5$  mM (Kinsman-Costello et al., 2017), with some of the variation in sulfate concentration due to hydrologically driven differences in mixing between alcove water and Lake Huron water. Given the relatively low sulfate concentrations at MIS and high availability of organic matter (Kinsman-Costello et al., 2017; Nold et al., 2013; Rico & Sheldon, 2019), sulfate is almost completely exhausted at depths of  $\sim 1$ –8cm (Figure 3; Kinsman-Costello et al., 2017) such that  $\delta^{34}\text{S}$  values of deep sulfide are similar to those of the overlying sulfate (Figure 5). Thus, sulfate concentrations at MIS are sufficiently low that progressive consumption of the sulfate reservoir dominates over differential metabolic activity in determining  $\delta^{34}\text{S}_{\text{sulfide}}$  patterns over cm scales.

Another important factor promoting consumption of the sulfate reservoir at MIS is organic matter. MIS hosts a thin ( $\sim 2$  mm) microbial mat overlying lake sediments. The sedimentary organic matter underlying the MIS mats has geochemical characteristics more similar to settling phytoplankton than the microbial mat biomass (Nold et al., 2013; Rico & Sheldon, 2019). Deep anaerobic communities are thus able to utilize labile planktonic biomass rather than microbial mat biomass, which can contain abundant cyanobacterial sheaths that are relatively resistant to microbial decay (Bartley, 1996; Horodyski et al., 1992). This enables sulfate reduction to exhaust the sulfate reservoir at depth, as is common in organic-rich marine sediments composed of labile planktonic biomass (e.g., Aller et al., 1996). In contrast, in the Guerrero Negro mats, high rates of organic matter remineralization at the surface consumes labile organic matter (Canfield & Des Marais, 1993), leaving mat material below composed primarily of degraded organic matter (Lee et al., 2019). Similarly, the organic matter below the  $\sim 1$ -cm-thick pigment-rich layer at the surface of the Little Ambergris Cay mats is composed of diagenetically altered, chemically recalcitrant organic matter (Gomes et al., 2020). The presence of degraded organic matter at depth may limit sulfate reduction, proving insufficient to fully consume the sulfate reservoir at depth in these other mat sites. Incomplete sulfate reduction may also be a result of microbial communities with sulfate transporters adapted to the high sulfate concentrations ( $>40$  mM) of these systems (Bradley et al., 2016). In sum, differences in  $\delta^{34}\text{S}_{\text{sulfide}}$  trends between MIS and previously studied mat sites can be attributed to sulfate reduction being limited by electron acceptors versus electron donors, respectively.

### 4.3 | Solid-phase sulfide $\delta^{34}\text{S}_{\text{sulfide}}$ signatures

Pyrite is a major geological archive of sulfide, and thus,  $\delta^{34}\text{S}$  values of pyrite and other sulfide minerals have been used to evaluate patterns of sulfur cycling and environmental conditions in ancient sediments

and microbial mats (see review in Fike et al., 2015). Here, we compare  $\delta^{34}\text{S}_{\text{sulfide}}$  patterns to  $\delta^{34}\text{S}$  values in two solid-phase sulfide pools: (1) acid-volatile sulfides (AVS), which are primarily composed of iron monosulfides that are an important intermediates in some pyrite formation pathways (Rickard, 2012; Rickard & Luther, 2007), and (2) chromium-reducible sulfides (CRS), which are primarily composed of pyrite and elemental sulfur (Canfield et al., 1986), with the latter potentially playing a role in the polysulfide pathway when elemental sulfur reacts with sulfide to form polysulfides (Rickard, 2012; Rickard & Luther, 2007). Trends in  $\delta^{34}\text{S}$  values differ between AVS, CRS, and porewater sulfide (Figure 6). AVS  $\delta^{34}\text{S}$  values are more variable (range from  $-7.3$  to  $18.5\text{\textperthousand}$ ,  $\sigma = 8.1\text{\textperthousand}$ ,  $n = 11$ ) than CRS  $\delta^{34}\text{S}$  values (range from  $-10.4$  to  $0.9\text{\textperthousand}$ ,  $\sigma = 3.9\text{\textperthousand}$ ,  $n = 14$ ). Trends in  $\delta^{34}\text{S}_{\text{AVS}}$  values with depth are somewhat similar to  $\delta^{34}\text{S}_{\text{sulfide}}$  trends;  $\delta^{34}\text{S}_{\text{AVS}}$  values are low below the SWI and increase with depth. However, only one measured  $\delta^{34}\text{S}_{\text{AVS}}$  value was within the range of high  $\delta^{34}\text{S}_{\text{sulfide}}$  values ( $\sim 15$  to  $18\text{\textperthousand}$ ) measured in the deep porewater (below 1.5 to 7.5 cm, depending on the time of day and mat type). Other  $\delta^{34}\text{S}_{\text{AVS}}$  values measured below 2.5 cm ranged from  $-0.1$  to  $9.9\text{\textperthousand}$ . There is a subtle increase in  $\delta^{34}\text{S}_{\text{CRS}}$  values with depth, but  $\delta^{34}\text{S}_{\text{CRS}}$  values remained between  $-10.4$  and  $0.9\text{\textperthousand}$ .

In order to improve interpretations of  $\delta^{34}\text{S}_{\text{CRS}}$  values preserved in ancient low-oxygen microbial mat environments, it is useful to explore how  $\delta^{34}\text{S}_{\text{CRS}}$  values relate to porewater  $\delta^{34}\text{S}_{\text{sulfide}}$  values. Porewater  $\delta^{34}\text{S}_{\text{sulfide}}$  values vary over diurnal cycles and vary between mat types. In contrast, sedimentary  $\delta^{34}\text{S}_{\text{CRS}}$  values represent a time-averaged signal because sediment accumulates at a rate of  $\sim 0.3$  g/cm $^2$ /year (Nold et al., 2013). It is also necessary to consider the timescale of change in mats at the SWI. The appearance of the mat (e.g., purple versus gray or white patches) varies over seasonal and annual timescales (Grim, 2019; cf., Nold et al., 2010; Voorhies et al., 2012, 2016; Kinsman-Costello et al., 2017). Thus, the sediment integrates  $\delta^{34}\text{S}$  signatures such that  $\delta^{34}\text{S}_{\text{CRS}}$  values represent an average of the geochemical conditions of sediment covered by different mat types, similar to other sedimentary environments (e.g., Houghton et al., 2019).

Spatial variability in solid-phase sulfide formation (i.e., AVS or CRS) can also impact  $\delta^{34}\text{S}_{\text{CRS}}$  and  $\delta^{34}\text{S}_{\text{AVS}}$  signatures. Previous work showed that there is not significant formation of pyrite in the sediment underlying the microbial mat. In particular, Rico and Sheldon (2019) reported iron speciation data from 9 cores sampled in October 2014 and June 2016 which showed no increase in pyrite concentrations with depth in the sediment (Figure 6). These results are consistent with our observation that  $\delta^{34}\text{S}_{\text{CRS}}$  values are similar to  $\delta^{34}\text{S}_{\text{sulfide}}$  values proximal to the microbial mat and indicate that  $\delta^{34}\text{S}_{\text{CRS}}$  values are primarily capturing  $\delta^{34}\text{S}_{\text{sulfide}}$  signatures near the SWI. There is a slight  $^{34}\text{S}$  enrichment (at most  $\sim 10\text{\textperthousand}$ ) in CRS with depth, which could be due to the minor additional CRS formation (i.e., pyrite or elemental sulfur) deeper in the sediment and inheritance of  $\delta^{34}\text{S}$  signatures of the corresponding sulfide, AVS, or polysulfides. Elemental sulfur produced from chemotrophic oxidation of sulfide is slightly  $^{34}\text{S}$ -enriched relative to the sulfide (e.g., Zerkle et al., 2016). Thus, the  $^{34}\text{S}$  enrichment in CRS with depth could be due to the incorporation of

$^{34}\text{S}$ -enriched elemental sulfur into the CRS pool and/or formation of pyrite via the polysulfide pathway with the  $^{34}\text{S}$ -enriched elemental sulfur serving as a polysulfide precursor. However, given that there is no increase in pyrite concentrations with depth, it is unlikely that the amount of additional pyrite formed over the studied depth interval (0 to ~20 cm) is greater than the relative uncertainty associated with the pyrite concentration analysis (replicate analyses have a relative standard deviation of ~12%; Rico & Sheldon, 2019). Further, decreases in AVS concentrations with depth in sediment have been shown to be due to dissolution of metastable iron monosulfide precipitates to aqueous iron monosulfides, rather than transformation of AVS to CRS (Rickard et al., 1999). Thus, although we cannot rule out that some AVS dissolves and then precipitates as pyrite in the deeper (>1 cm) sediment, we lack evidence for substantial pyrite formation at depth (Figure 6; Rico & Sheldon, 2019). Thus, the CRS pool, which is likely to be the most geologically stable sulfide pool, is primarily formed near the microbial mat at the SWI and captures  $\delta^{34}\text{S}$  signature sulfide in that location.

Sulfur cycling within the mat may play a role in promoting pyrite formation near the SWI. Both sulfate-reducing and sulfide-oxidizing taxa have been documented in the surface mat (Nold et al., 2010) and sediments (0–3 cm; Kinsman-Costello et al., 2017). Various types of sulfide oxidation processes produce  $\text{S}^0$  or other sulfur intermediates near the mat surface. In particular, anoxygenic photosynthetic cyanobacteria at MIS produce these sulfur intermediates and immediately secrete them to their surroundings (Nold et al., 2010). These intermediate sulfur species can react with sulfide to form polysulfides, which promote CRS formation via the polysulfide pathway (eqn. 2; Rickard, 1975; Rickard & Luther, 2007). Besides producing intermediate sulfur species, experimental studies have shown that other activities of microorganisms can promote pyrite formation. The formation of iron sulfide precursors to pyrite can occur on cell surfaces of sulfate-reducing microorganisms (Picard et al., 2018). Pyrite formation can also be coupled to methane production in microbial cultures containing sulfate-reducing bacteria and methanogens (Thiel et al., 2019). In Santa Barbara Basin, it was proposed that pyrite formed in biofilms rather than in sedimentary pore waters (Raven et al., 2016). Thus, although iron geochemistry may have played a role in limiting the depth interval over which pyrite formation could occur (Rico & Sheldon, 2019), it is likely that the production of sulfur intermediates that could react with sulfide to form polysulfide and other microbial activity also played a role in promoting pyrite formation near the SWI.

These results have implications for studies of both bulk and high-spatial resolution sedimentary sulfur isotope geochemistry of sediments interpreted to be formed in microbial mat environments (e.g. Fischer et al., 2014; Gomes et al., 2018; Meyer et al., 2017; Wacey et al., 2010). Specifically, our results and iron speciation data (Rico & Sheldon, 2019) indicate that pyrite formation primarily occurs near the surface microbial mat (within the top 1 cm), where microbial activity can promote pyrite formation. Therefore, in systems such as MIS,  $\delta^{34}\text{S}_{\text{CRS}}$  values preserve information about environmental

conditions at the mat surface and are only minimally influenced by early diagenetic processes that affect deeper portions of the sediment. This is in part due to iron geochemistry that is unfavorable to further CRS precipitation in deeper portions of the mat, as indicated by invariant pyrite concentrations (Figure 6) and iron speciation with depth in the sediment (Rico & Sheldon, 2019). In ancient oceans with more abundant iron, it is possible that iron geochemistry more favorable to CRS formation could have extended the zone of CRS formation deeper into the sediment, resulting in the incorporation of deeper sulfide and/or AVS into early diagenetic pyrite. Of course, later diagenetic processes can also affect  $\delta^{34}\text{S}_{\text{CRS}}$  values, and therefore, petrography or additional chemical tools should be used to assess evidence for further post-depositional sulfide formation or transformation. Petrographically constrained micro-scale  $\delta^{34}\text{S}_{\text{pyrite}}$  analyses can be used to infer different phases of sulfide formation, as well as other phases of post-depositional metal sulfide formation and/or recrystallization, especially when done in conjunction with other high-spatial resolution geochemical analyses (e.g. Bryant et al., 2019; Cui et al., 2018; Fischer et al., 2014; Gomes et al., 2018; Meyer et al., 2017; Wacey et al., 2010). These studies can be used to discern whether sulfur cycling within ancient mat environments was more similar to those documented in higher sulfate (>28 mM) environments dominated by recalcitrant cyanobacterial biomass (Fike et al., 2008, 2009; Gomes et al., 2020; Lee et al., 2019) or in mats such as MIS characterized by planktonic-sourced organic matter and substantial consumption of the ambient sulfate reservoir.

In the low-oxygen system at MIS, low sulfate concentrations (~ $7.1 \pm 1.5$  mM; Kinsman-Costello et al., 2017) result in sulfur isotope geochemistry dominated by progressive consumption of the sulfate reservoir rather than differential metabolic activity. The diurnal  $\delta^{34}\text{S}_{\text{sulfide}}$  variability is shaped by both geomicrobiological cycling in the surface mat and the activities of migrating diatoms. This style of geomicrobiological cycling is not known to be common in the modern ocean, and it is unclear if it was common in the past. Therefore, it is not our intention to imply that similar migratory activity shaped  $\delta^{34}\text{S}_{\text{sulfide}}$  trends in ancient oceans dominated by microbial mat ecosystems. Whatever taxa were present in ancient microbial mat ecosystems, electron-donor versus electron-acceptor limitation would have impacted  $\delta^{34}\text{S}_{\text{sulfide}}$  trends (i.e., if they are driven by differential metabolic activity versus progressive consumption of the sulfate reservoir) and iron geochemistry would have impacted the location of pyrite formation. At MIS, low sulfate concentrations (~ $7.1 \pm 1.5$  mM), labile planktonic biomass, and iron geochemistry all result in early diagenetic pyrite that captures  $\delta^{34}\text{S}$  signatures of pore water sulfide near the SWI of the low-oxygen microbial mat.

## 5 | CONCLUSIONS

Geomicrobiological cycling in low-oxygen microbial mats at Middle Island Sinkhole results in dynamic  $\delta^{34}\text{S}_{\text{sulfide}}$  patterns over diurnal cycles that span depths well below the microbial mats. The diurnal

cycles primarily affect  $\delta^{34}\text{S}_{\text{sulfide}}$  values near the sediment–water interface, where  $\delta^{34}\text{S}_{\text{sulfide}}$  values range from  $-7.1$  to  $11.1\text{‰}$ . The availability of oxidants and transport of oxidants by migrating taxa have cascading effects on net sulfate reduction rates deeper in the sediment. The consumption of the sulfate reservoir in deeper sediments results in  $\delta^{34}\text{S}_{\text{sulfide}}$  trends where sulfide is  $^{34}\text{S}$ -depleted at the surface and becomes  $^{34}\text{S}$ -enriched with depth, approaching  $\delta^{34}\text{S}$  values of the overlying sulfate reservoir. Despite the dynamic diurnal  $\delta^{34}\text{S}_{\text{sulfide}}$  patterns, pyrite captures  $\delta^{34}\text{S}$  signatures of the ambient sulfide at the locus of its formation at or immediately adjacent to the surface microbial mat. Thus, the chromium-reducible sulfur pool, usually considered to be composed primarily of pyrite, captures  $\delta^{34}\text{S}$  signatures near the sediment–water interface and is only minimally altered by deeper early diagenetic processes. In addition to the role of the low-oxygen microbial mat communities, these  $\delta^{34}\text{S}$  patterns are also likely due to a relatively low sulfate concentrations ( $\sim 7\text{ mM}$ ), inputs of labile planktonic biomass, and limited iron availability. These results, and their contrast with those from other mat systems in distinct geochemical and environmental settings such as Guerrero Negro, have implications for the interpretations of both bulk and fine-scale studies of  $\delta^{34}\text{S}$  signatures of pyrite in sediments formed in microbial mat environments. Specifically, bulk  $\delta^{34}\text{S}$  values will integrate  $\delta^{34}\text{S}_{\text{sulfide}}$  signals over the location of pyrite formation, which is primarily the mat surface at MIS. Microanalytical studies of  $\delta^{34}\text{S}$  values of pyrite may document individual pyrite grains with  $\delta^{34}\text{S}$  values that span the range of  $\delta^{34}\text{S}_{\text{sulfide}}$  values at the mat surface with a mean  $\delta^{34}\text{S}$  value corresponding to the bulk pyrite  $\delta^{34}\text{S}$  value.

## ACKNOWLEDGMENTS

We thank the NOAA Thunder Bay National Marine Sanctuary Dive Unit—John Bright, Russ Green, Phil Hartmeyer, Wayne Lusardi, Stephanie Gandulla, Katie Clevenger, and Annie Wright—and R/V Storm Ship Captain Travis Smith for field support, site access, and sampling. We also thank Dirk de Beer, Arjun Chennu, Bopaliah Biddanda, Dack Stuart, Greg Druschel, Martin Kurek, Chase Howard, John Shukle, Hui Chien Tan, and Heidi Babos for help with field science operations and useful conversation and Stephanie Moore for laboratory and technical assistance. This work was supported by NSF grant EAR-1637066 to G.J.D. and W.Z.

## DATA AVAILABILITY STATEMENT

The data that support the findings of this study are available in the supplementary material of this article.

## ORCID

Maya L. Gomes  <https://orcid.org/0000-0002-9707-350X>  
 Judith M. Klatt  <https://orcid.org/0000-0002-0195-6333>  
 Gregory J. Dick  <https://orcid.org/0000-0001-7666-6288>  
 Kathryn I. Rico  <https://orcid.org/0000-0003-2761-8663>  
 Lauren Kinsman-Costello  <https://orcid.org/0000-0002-9168-8677>  
 Nathan D. Sheldon  <https://orcid.org/0000-0003-3371-0036>  
 David A. Fike  <https://orcid.org/0000-0003-2848-0328>

## REFERENCES

Aller, R. C., Blair, N. E., Xia, Q., & Rude, P. D. (1996). Remineralization rates, recycling, and storage of carbon in Amazon shelf sediments. *Continental Shelf Research*, 16, 753–786. [https://doi.org/10.1016/0278-4343\(95\)00046-1](https://doi.org/10.1016/0278-4343(95)00046-1)

Balci, N., Shanks, W. C., Mayer, B., & Mandernack, K. W. (2007). Oxygen and sulfur isotope systematics of sulfate produced by bacterial and abiotic oxidation of pyrite. *Geochimica et Cosmochimica Acta*, 71, 3796–3811. <https://doi.org/10.1016/j.gca.2007.04.017>

Bao, H. (2006). Purifying barite for oxygen isotope measurement by dissolution and reprecipitation in a chelating solution. *Analytical Chemistry*, 78, 304–309. <https://doi.org/10.1021/ac051568z>

Bartley, J. K. (1996). Actualistic taphonomy of cyanobacteria: Implications for the Precambrian fossil record. *Palaios*, 11, 571–586. <https://doi.org/10.2307/3515192>

Biddanda, B. A., Coleman, D. F., Johengen, T. H., Ruberg, S. A., Meadows, G. A., Van Sumeren, H. W., Rediske, R. R., & Kendall, S. T. (2006). Exploration of a submerged sinkhole ecosystem in Lake Huron. *Ecosystems*, 9, 828–842. <https://doi.org/10.1007/s10021-005-0057-y>

Biddanda, B. A., McMillan, A. C., Long, S. A., Snider, M. J., & Weinke, A. D. (2015). Seeking sunlight: rapid phototactic motility of filamentous mat-forming cyanobacteria optimize photosynthesis and enhance carbon burial in Lake Huron's submerged sinkholes. *Frontiers in Microbiology*, 6, 1–13. <https://doi.org/10.3389/fmicb.2015.00930>

Biddanda, B. A., & Weinke, A. D. accepted. Extant mat world analog microbes synchronize migration to a diel tempo. *Limnology and Oceanography*, <https://doi.org/10.1002/essoar.10502762.10502761>

Bottcher, M. E., Thamdrup, B., & Vennemann, T. W. (2001). Oxygen and sulfur isotope fractionation during anaerobic bacterial disproportionation of elemental sulfur. *Geochimica et Cosmochimica Acta*, 65, 1601–1609. [https://doi.org/10.1016/S0016-7037\(00\)00628-1](https://doi.org/10.1016/S0016-7037(00)00628-1)

Bradley, A. S., Leavitt, W. D., Schmidt, M., Knoll, A. H., Girguis, P. R., & Johnston, D. T. (2016). Patterns of sulfur isotope fractionation during microbial sulfate reduction. *Geobiology*, 14(1), 91–101. <https://doi.org/10.1111/gbi.12149>

Bryant, R. N., Jones, C., Raven, M. R., Gomes, M. L., Berelson, W. M., Bradley, A. S., & Fike, D. A. (2019). Sulfur isotope analysis of microcrystalline iron sulfides using secondary ion mass spectrometry imaging: Extracting local paleo-environmental information from modern and ancient sediments. *Rapid Communications in Mass Spectrometry*, 33, 491–502. <https://doi.org/10.1002/rcm.8375>

Cahoon, L. (1999). The role of benthic microalgae in neritic ecosystems. *Oceanography and Marine Biology*, 37, 47–86.

Canfield, D. E., & Des Marais, D. J. (1993). Biogeochemical cycles of carbon, sulfur, and free oxygen in a microbial mat. *Geochimica et Cosmochimica Acta*, 57, 3971–3984. [https://doi.org/10.1016/0016-7037\(93\)90347-Y](https://doi.org/10.1016/0016-7037(93)90347-Y)

Canfield, D. E., & Farquhar, J. (2009). Animal evolution, bioturbation, and the sulfate concentration of the oceans. *Proceedings of the National Academy of Science*, 106, 8123–8127. <https://doi.org/10.1073/pnas.0902037106>

Canfield, D. E., Farquhar, J., & Zerkle, A. L. (2010). High isotope fractionations during sulfate reduction in a low-sulfate euxinic ocean analog. *Geology*, 38, 415–418.

Canfield, D. E., Raiswell, R. R., Westrich, J. T., Reaves, C. M., & Berner, R. A. (1986). The use of chromium reduction in the analysis of reduced inorganic sulfur in sediments and shales. *Chemical Geology*, 54, 149–155. [https://doi.org/10.1016/0009-2541\(86\)90078-1](https://doi.org/10.1016/0009-2541(86)90078-1)

Cartaxana, P., Brotas, V., & Serôdio, J. (2008). Effects of two motility inhibitors on the photosynthetic activity of the diatoms cylindrotheca closterium and pleurosigma angulatum. *Diatom Research*, 23, 65–74.

Chanton, J. P., & Martens, C. S. (1985). The effects of heat and stannous chloride addition on the active distillation of acid volatile sulfide from pyrite-rich marine sediment samples. *Biogeochemistry*, 1(4), 375–382. <https://doi.org/10.1007/BF02187379>

Cui, H., Kitajima, K., Spicuzza, M. J., Fournelle, J. H., Denny, A., Ishida, A., Zhang, F., & Valley, J. W. (2018). Questioning the biogenicity of Neoproterozoic superheavy pyrite by SIMS. *American Mineralogist*, 103, 1362–1400. <https://doi.org/10.2138/am-2018-6489>

de Beer, D., Glud, A., Epping, E., & Kiihl, M. (1997). A fast-responding CO<sub>2</sub> microelectrode for profiling sediments, microbial mats, and biofilms. *Limnology and Oceanography*, 42, 1590–1600.

Des Marais, D. J. (2003). Biogeochemistry of hypersaline microbial mats illustrates the dynamics of modern microbial ecosystems and the early evolution of the biosphere. *Biology Bulletin*, 204, 160–167. <https://doi.org/10.2307/1543552>.

Dick, G. J., Grim, S. L., & Klatt, J. M. (2018). Controls on O<sub>2</sub> production in cyanobacterial mats and implications for earth's oxygenation. *Annual Review of Earth and Planetary Sciences*, 46, 123–147.

Donald, R., & Southam, G. (1999). Low temperature anaerobic bacterial diagenesis of ferrous monosulfide to pyrite. *Geochimica et Cosmochimica Acta*, 63, 2019–2023. [https://doi.org/10.1016/S0016-7037\(99\)00140-4](https://doi.org/10.1016/S0016-7037(99)00140-4)

Dunker, R., Roy, H., Kamp, A., & Jorgensen, B. B. (2011). Motility patterns of filamentous sulfur bacteria, *Beggiatoa* spp. *FEMS Microbiology Ecology*, 77(1), 176–185. <https://doi.org/10.1111/j.1574-6941.2011.01099.x>

Fike, D. A., Bradley, A. S., & Rose, C. V. (2015). Rethinking the ancient sulfur cycle. *Annual Review of Earth and Planetary Sciences*, 43(1), 593–622. <https://doi.org/10.1146/annurev-earth-060313-054802>

Fike, D. A., Finke, N., Zha, J., Blake, G., Hoehler, T. M., & Orphan, V. J. (2009). The effect of sulfate concentration on (sub)millimeter-scale sulfide δ<sup>34</sup>S in hypersaline cyanobacterial mats over the diurnal cycle. *Geochimica et Cosmochimica Acta*, 73, 6187–6204. <https://doi.org/10.1016/j.gca.2009.07.006>

Fike, D. A., Gammon, C. L., Ziebis, W., & Orphan, V. J. (2008). Micron-scale mapping of sulfur cycling across the oxycline of a cyanobacterial mat: A paired nanoSIMS and CARD-FISH approach. *ISME Journal*, 2(7), 749–759. <https://doi.org/10.1038/ismej.2008.39>

Fike, D. A., Houghton, J. L., Moore, S. E., Gilhooly, W. P., Dawson, K. S., Druschel, G. K., Amend, J. P., & Orphan, V. J. (2017). Spatially resolved capture of hydrogen sulfide from the water column and sedimentary pore waters for abundance and stable isotopic analysis. *Marine Chemistry*, 197, 26–37. <https://doi.org/10.1016/j.marchem.2017.10.004>

Fischer, W. W., Fike, D. A., Johnson, J. E., Raub, T. D., Guan, Y., Kirschvink, J. L., & Eiler, J. M. (2014). SQUID-SIMS is a useful approach to uncover primary signals in the Archean sulfur cycle. *Proceedings of the National Academy of Science*, 111, 5468–5473. <https://doi.org/10.1073/pnas.1322577111>

Fossing, H., & Jørgensen, B. B. (1989). Measurements of bacterial sulphate reduction in sediments: Evaluation of a single-step chromium reduction method. *Biogeochemistry*, 8, 205–222.

Gomes, M. L., Fike, D. A., Bergmann, K. D., Jones, C., & Knoll, A. H. (2018). Environmental insights from high-resolution (SIMS) sulfur isotope analyses of sulfides in Proterozoic microbialites with diverse mat textures. *Geobiology*, 16, 17–34. <https://doi.org/10.1111/gbi.12265>

Gomes, M. L., & Hurtgen, M. T. (2013). Sulfur isotope systematics of a euxinic, low-sulfate lake: Evaluating the importance of the reservoir effect in modern and ancient oceans. *Geology*, 41, 6, 663–666. <https://doi.org/10.1130/G34187.1>

Gomes, M. L., & Hurtgen, M. T. (2015). Sulfur isotope fractionation in modern euxinic systems: Implications for paleoenvironmental reconstructions of paired sulfate–sulfide isotope records. *Geochimica et Cosmochimica Acta*, 157, 39–55. <https://doi.org/10.1016/j.gca.2015.02.031>

Gomes, M. L., & Johnston, D. T. (2017). Oxygen and sulfur isotopes in sulfate in modern euxinic systems with implications for evaluating the extent of euxinia in ancient oceans. *Geochimica et Cosmochimica Acta*, 205, 331–359. <https://doi.org/10.1016/j.gca.2017.02.020>

Gomes, M., Reidman, L. A., O'Reilly, S. S., Lingappa, U., Metcalfe, K., Fike, D. A., Grotzinger, J. P., Fischer, W. W., & Knoll, A. H. (2020). Microbial Mats on little ambergris cay. Turks and caicos islands: taphonomy and the selective preservation of biosignatures. *Frontiers in Earth Sciences*, 8, 387.

Grim, S. L. (2019). *Genomic and Functional Investigations Into Seasonally-Impacted and Morphologically-Distinct Anoxygenic Photosynthetic Cyanobacterial Mats* [PhD: University of Michigan.

Grotzinger, J. P., & Knoll, A. H. (1999). Stromatolites in precambrian carbonates: Evolutionary mileposts or environmental dipsticks? *Annual Review of Earth and Planetary Sciences*, 27, 313–358. <https://doi.org/10.1146/annurev.earth.27.1.313>

Guarini, J.-M., Chauvaud, L., & Coston-Guarini, J. (2009). Can the intertidal benthic microalgal primary production account for the "Missing Carbon Sink"? *Journal of Oceanography Research and Data*, 1, 13–19.

Habicht, K. S., & Canfield, D. E. (1997). Sulfur isotope fractionation during bacterial sulfate reduction in organic-rich sediments. *Geochimica et Cosmochimica Acta*, 61, 5351–5361. [https://doi.org/10.1016/S0016-7037\(97\)00311-6](https://doi.org/10.1016/S0016-7037(97)00311-6)

Harrison, A. G., & Thode, H. G. (1958). Mechanism of the bacterial reduction of sulphate from isotope fractionation studies. *Transactions of the Faraday Society*, 54(1), 84–92. <https://doi.org/10.1039/tf9585400084>

Horodyski, R. J., Bauld, J., Lipps, J. H., & Mendelson, C. V. (1992). Preservation of prokaryotes and organic-walled and calcareous and siliceous protists. In J. W. Schopf, & C. Klein (Eds.), *The proterozoic biosphere: A multidisciplinary study* (pp. 185–193). Cambridge University Press.

Houghton, J. L., Gilhooly, W. P., Kafantaris, F.-C.-A., Druschel, G. K., Lu, G.-S., Amend, J. P., Godelitsas, A., & Fike, D. A. (2019). Spatially and temporally variable sulfur cycling in shallow-sea hydrothermal vents, Milos, Greece. *Marine Chemistry*, 208, 83–94. <https://doi.org/10.1016/j.marchem.2018.11.002>

Huerta-Diaz, M. A., Delgadillo-Hinojosa, F., Otero, X. L., Segovia-Zavala, J. A., Hernandez-Ayon, J. M., Galindo-Bect, M. S., & Amaro-Franco, E. (2011). Iron and trace metals in microbial mats and underlying sediments: Results from Guerrero Negro Saltern, Baja California Sur, Mexico. *Aquatic Geochemistry*, 17, 603–628. <https://doi.org/10.1007/s10498-011-9126-3>

Jeroschewski, P., Steuckart, C., & Kuhl, M. (1996). An amperometric microsensor for the determination of H<sub>2</sub>S in aquatic environments. *Analytical Chemistry*, 68, 4351–4357.

Jørgensen, B. B. (1978). A comparison of methods for the quantification of bacterial sulphate reduction in coastal marine sediments: I. Measurements with radiotracer techniques. *Geomicrobiology Journal*, 1, 11–27.

Jørgensen, B. B. (1979). A theoretical model of the stable sulfur isotope distribution in marine sediments. *Geochimica et Cosmochimica Acta*, 43, 363–374. [https://doi.org/10.1016/0016-7037\(79\)90201-1](https://doi.org/10.1016/0016-7037(79)90201-1)

Kallmeyer, J., Ferdelman, T. G., Weber, A., Fossing, H., & Jørgensen, B. B. (2004). A cold chromium distillation procedure for radiolabeled sulfide applied to sulfate reduction measurements. *Limnology and Oceanography: Methods*, 2, 171–180. <https://doi.org/10.4319/lom.2004.2.171>

Kamp, A., de Beer, D., Nitsch, J. L., Lavik, G., and Stief, P. (2011). Diatoms respire nitrate to survive dark and anoxic conditions: Proceedings of the National Academy of Sciences, 108, 5649–5654.

Kallmeyer, J., Ferdelman, T. G., Weber, A., Fossing, H., & Jørgensen, B. B. (2004). A cold chromium distillation procedure for radiolabeled sulfide applied to sulfate reduction measurements. *Limnology and*

Oceanography: Methods, 2, 171–180. <https://doi.org/10.4319/lom.2004.2.171>

Kamp, A., de Beer, D., Nitsch, J. L., Lavik, G., and Stief, P., 2011. Diatoms respire nitrate to survive dark and anoxic conditions: *Proceedings of the National Academy of Sciences*, 108, 5649–5654.

Kamp, A., de Beer, D., Nitsch, J. L., Lavik, G., & Stief, P. (2011). Diatoms respire nitrate to survive dark and anoxic conditions. *Proceedings of the National Academy of Sciences*, 108, 5649–5654. <https://doi.org/10.1073/pnas.1015744108>

Kaplan, I. R., & Rittenberg, S. C. (1964). Microbiological fractionation of sulphur isotopes. *Journal of General Microbiology*, 34, 195–212. <https://doi.org/10.1099/00221287-34-2-195>

Kinsman-Costello, L. E., Sheik, C. S., Sheldon, N. D., Allen Burton, G., Costello, D. M., Marcus, D., Uyl, P. A., & Dick, G. J. (2017). Groundwater shapes sediment biogeochemistry and microbial diversity in a submerged Great Lake sinkhole. *Geobiology*, 15(2), 225–239. <https://doi.org/10.1111/gbi.12215>

Kjeldsen, K. U., Schreiber, L., Thorup, C. A., Boesen, T., Bjerg, J. T., Yang, T., Dueholm, M. S., Larsen, S., Risgaard-Petersen, N., Nierychlo, M., Schmid, M., Bøggild, A., Vossenberg, J. D., Geelhoed, J. S., Meysman, F. J. R., Wagner, M., Nielsen, P. H., Nielsen, L. P., & Schramm, A. (2019). On the evolution and physiology of cable bacteria. *Proceedings of the National Academy of Sciences United States of America*, 116, 19116–19125. <https://doi.org/10.1073/pnas.1903514116>

Clatt, J. M., Marchant, H., de Beer, D., Ziebis, W., Druschel, G., Medina, M., Chennu, A., & Dick, G. (2017). Response of Chemotrophic Processes to Dynamic Redox Conditions in a Cyanobacterial Mat: 27th Goldschmidt Conference, Paris, France, August 2017.

Clatt, J. M., & Polerecky, L. (2015). Assessment of the stoichiometry and efficiency of CO<sub>2</sub> fixation coupled to reduced sulfur oxidation. *Frontiers in Microbiology*, 6, 484. <https://doi.org/10.3389/fmicb.2015.00484>

Krekeler, D., Teske, A., & Cypionka, H. (1998). Strategies of sulfate-reducing bacteria to escape oxygen stress in a cyanobacterial mat. *FEMS Microbiology Ecology*, 25, 89–96. <https://doi.org/10.1111/j.1574-6941.1998.tb00462.x>

Leavitt, W. D., Halevy, I., Bradley, A. S., & Johnston, D. T. (2013). Influence of sulfate reduction rates on the Phanerozoic sulfur isotope record. *Proceedings of the National Academy of Sciences United States of America*, 110(28), 11244–11249. <https://doi.org/10.1073/pnas.1218874110>

Lee, C., Love, G. D., Jahnke, L. L., Kubo, M. D., & Des Marais, D. J. (2019). Early diagenetic sequestration of microbial mat lipid biomarkers through covalent binding into insoluble macromolecular organic matter (IMOM) as revealed by sequential chemolysis and catalytic hydrolysis. *Organic Geochemistry*, 132, 11–22. <https://doi.org/10.1016/j.orggeochem.2019.04.002>

Lenton, T. M., & Daines, S. J. (2017). Matworld – the biogeochemical effects of early life on land. *New Phytologist*, 215, 531–537. <https://doi.org/10.1111/nph.14338>

Longphuirt, S., Lim, J.-H., Leynaert, A., Claquin, P., Choy, E.-J., Kang, C.-K., & An, S. (2009). Dissolved inorganic nitrogen uptake by intertidal microphytobenthos: Nutrient concentrations, light availability and migration. *Marine Ecology Progress Series*, 379, 33–34. <https://doi.org/10.3354/meps07852>

Luther, G. W. (2005). Acid volatile sulfide – A comment. *Marine Chemistry*, 97, 198–205. <https://doi.org/10.1016/j.marchem.2005.08.001>

Lyons, T. W. (1997). Sulfur isotopic trends and pathways of iron sulfide formation in upper Holocene sediments of the Black Sea. *Geochimica et Cosmochimica Acta*, 61, 3367–3382.

Lyons, T. W., Anbar, A. D., Severmann, S., Scott, C., & Gill, B. C. (2009). Tracking Euxinia in the ancient ocean: A multiproxy perspective and proterozoic case study. *Annual Review of Earth and Planetary Sciences*, 37, 507–534. <https://doi.org/10.1146/annurev.earth.36.031207.124233>

Macintyre, H., Geider, R., & Miller, D. (1996). Microphytobenthos: The ecological role of the "Secret Garden" of unvegetated, shallow-water marine habitats. I. Distribution, abundance and primary production. *Estuaries and Coasts*, 19, 186–201. <https://doi.org/10.2307/1352224>

Malkin, S. Y., Rao, A. M., Seitaj, D., Vasquez-Cardenas, D., Zetsche, E.-M., Hidalgo-Martinez, S., Boschker, H. T., & Meysman, F. J. (2014). Natural occurrence of microbial sulphur oxidation by long-range electron transport in the seafloor. *ISME Journal*, 8, 1843–1854. <https://doi.org/10.1038/ismej.2014.41>

Mandernack, K. W., Krouse, H. R., & Skei, J. M. (2003). A stable sulfur and oxygen isotopic investigation of sulfur cycling in an anoxic marine basin, Framvaren Fjord, Norway. *Chemical Geology*, 195, 181–200. [https://doi.org/10.1016/S0009-2541\(02\)00394-7](https://doi.org/10.1016/S0009-2541(02)00394-7)

Mariotti, A., Germon, J. C., Hubert, P., Kaiser, P., Leto Ile, R., Tardieu, A., & Tardieu, P. (1981). Some principles; illustration for the denitrification and nitrification processes. *Plant and Soil*, 62, 413–430. <https://doi.org/10.1007/BF02374138>

Merz, E., Dick, G. J., de Beer, D., Grim, S., Hübener, T., Littmann, S., Olsen, K., Stuart, D., Lavik, G., Marchant, H. K., & Klatt, J. M. (2020). Nitrate respiration and diel migration patterns of diatoms are linked in sediments underneath a microbial mat. *Environmental Microbiology*, 23(3), 1422–1435. <https://doi.org/10.1111/1462-2920.15345>

Meyer, N. R., Zerkle, A. L., & Fike, D. A. (2017). Sulphur cycling in a Neoproterozoic microbial mat. *Geobiology*, 15(3), 353–365. <https://doi.org/10.1111/gbi.12227>

Nakai, N., & Jensen, M. L. (1964). The kinetic isotope effect in the bacterial reduction and oxidation of sulfur. *Geochimica et Cosmochimica Acta*, 28, 1893–1912. [https://doi.org/10.1016/0016-7037\(64\)90136-X](https://doi.org/10.1016/0016-7037(64)90136-X)

Nielsen, L. P., Risgaard-Petersen, N., Fossing, H., Christensen, P. B., & Sayama, M. (2010). Electric currents couple spatially separated biogeochemical processes in marine sediment. *Nature*, 463(7284), 1071–1074. <https://doi.org/10.1038/nature08790>

Nold, S. C., Bellecourt, M. J., Kendall, S. T., Ruberg, S. A., Sanders, T. G., Klump, J. V., & Biddanda, B. A. (2013). Underwater sinkhole sediments sequester Lake Huron's carbon. *Biogeochemistry*, 115, 235–250. <https://doi.org/10.1007/s10533-013-9830-8>

Nold, S. C., Pangborn, J. B., Zajack, H. A., Kendall, S. T., Rediske, R. R., & Biddanda, B. A. (2010). Benthic bacterial diversity in submerged sinkhole ecosystems. *Applied and Environmental Microbiology*, 76, 347–351. <https://doi.org/10.1128/AEM.01186-09>

Nold, S. C., Zajack, H. A., & Biddanda, B. A. (2010). Eukaryal and archaeal diversity in a submerged sinkhole ecosystem influenced by sulfur-rich, hypoxic groundwater. *Journal of Great Lakes Research*, 36, 366–375. <https://doi.org/10.1016/j.jglr.2010.02.014>

Pasquier, V., Sansjofre, P., Rabineau, M., Revillon, S., Houghton, J., & Fike, D. A. (2017). Pyrite sulfur isotopes reveal glacial-interglacial environmental changes. *Proceedings of the National Academy of Sciences United States of America*, 114(23), 5941–5945. <https://doi.org/10.1073/pnas.1618245114>

Pellerin, A., Antler, G., Holm, S. A., Findlay, A. J., Crockford, P. W., Turchyn, A. V., Jørgensen, B. B., & Finster, K. (2019). Large sulfur isotope fractionation by bacterial sulfide oxidation: *Science Advances*, 5, eaaw1480. <https://doi.org/10.1126/sciadv.aaw1480>

Peters, S. E., Husson, J. M., & Wilcots, J. (2017). The rise and fall of stromatolites in shallow marine environments. *Geology*, 45(6), 487–490. <https://doi.org/10.1130/G38931.1>

Pfeffer, C., Larsen, S., Song, J., Dong, M., Besenbacher, F., Meyer, R. L., Kjeldsen, K. U., Schreiber, L., Gorby, Y. A., El-Naggar, M. Y., Leung, K. M., Schramm, A., Risgaard-Petersen, N., & Nielsen, L. P. (2012). Filamentous bacteria transport electrons over centimetre distances. *Nature*, 491, 218–221. <https://doi.org/10.1038/nature11586>

Picard, A., Gartman, A., Clarke, D. R., & Grguis, P. R. (2018). Sulfate-reducing bacteria influence the nucleation and growth of mackinawite and greigite. *Geochimica et Cosmochimica Acta*, 220, 367–384. <https://doi.org/10.1016/j.gca.2017.10.006>

Pinckney, J., & Zingmark, R. G. (1991). Effects of tidal stage and sun angles on intertidal benthic microalgal productivity. *Marine Ecology Progress Series*, 76, 81–89. <https://doi.org/10.3354/meps076081>

Present, T. M., Trower, L., Stein, N., Alleon, J., Bahniuk, A., Gomes, M. L., Lingappa, U., Metcalfe, K., Orzechowski, E. A., Riedman, L. A., Sanders, C. B., Morris, D. K., O'Reilly, S., Sibert, E. C., Thorpe, M., Tarika, M., Fischer, W. W., Knoll, A. H., & Grotzinger, J. P. (2018). *Sedimentology and Geochemistry of Ooid Sands Buried Beneath Microbial Mats, Little Ambergris Cay, Turks and Caicos Islands*. American Association of Petroleum Geologists Annual Convention & Exhibition.

Raven, M. R., Sessions, A. L., Fischer, W. W., & Adkins, J. F. (2016). Sedimentary pyrite d34S differs from porewater sulfide in Santa Barbara Basin: Proposed role of organic sulfur. *Geochimica et Cosmochimica Acta*, 186, 120–134.

Revsbech, N. P. (1989). An oxygen microsensor with a guard cathode. *Limnology and Oceanography*, 34, 474–478. <https://doi.org/10.4319/lo.1989.34.2.00474>

Revsbech, N. P., Jorgensen, B. B., Blackburn, T. H., & Cohen, Y. (1983). Microelectrode studies of the photosynthesis and O<sub>2</sub>, H<sub>2</sub>S, and pH profiles of a microbial mat1. *Limnology and Oceanography*, 26, 1062–1074.

Rickard, D. T. (1975). Kinetics and mechanism of pyrite formation at low temperatures. *American Journal of Science*, 275, 636–652. <https://doi.org/10.2475/ajs.275.6.636>

Rickard, D. T. (1997). Kinetics of pyrite formation by the H<sub>2</sub>S oxidation of iron (II) monosulfide in aqueous solutions between 25 and 125°C: The rate equation. *Geochimica et Cosmochimica Acta*, 61, 115–134. [https://doi.org/10.1016/S0016-7037\(96\)00321-3](https://doi.org/10.1016/S0016-7037(96)00321-3)

Rickard, D. T. (2012). *Sulfidic sediments and sedimentary rocks*. Elsevier.

Rickard, D., Butler, I. B., & Oldroyd, A. (2001). A novel iron sulphide mineral switch and its implications for Earth and planetary science. *Earth and Planetary Science Letters*, 189, 85–91. [https://doi.org/10.1016/S0012-821X\(01\)00352-1](https://doi.org/10.1016/S0012-821X(01)00352-1)

Rickard, D., Grimes, S., Butler, I., Oldroyd, A., & Davies, K. L. (2007). Botanical constraints on pyrite formation. *Chemical Geology*, 236, 228–246. <https://doi.org/10.1016/j.chemgeo.2006.09.011>

Rickard, D. T., & Luther, G. W. (1997). Kinetics of pyrite formation by the H<sub>2</sub>S oxidation of iron (II) monosulfide in aqueous solutions between 25 and 125°C: The mechanism. *Geochimica et Cosmochimica Acta*, 61, 135–147. [https://doi.org/10.1016/S0016-7037\(96\)00322-5](https://doi.org/10.1016/S0016-7037(96)00322-5)

Rickard, D., & Luther, G. W. (2007). Chemistry of iron sulfides. *Chemical Reviews*, 107, 514–562. <https://doi.org/10.1021/cr0503658>

Rickard, D., & Morse, J. W. (2005). Acid volatile sulfide (AVS). *Marine Chemistry*, 97, 141–197. <https://doi.org/10.1016/j.marchem.2005.08.004>

Rickard, D. T., Oldroyd, A., & Cramp, A. (1999). Voltammetric evidence for soluble FeS complexes in anoxic estuarine muds. *Estuaries*, 22, 693–701. <https://doi.org/10.2307/1353056>

Rico, K. I., & Sheldon, N. D. (2019). Nutrient and iron cycling in a modern analogue for the redoxcline of a Proterozoic ocean shelf. *Chemical Geology*, 511, 42–50. <https://doi.org/10.1016/j.chemgeo.2019.02.032>

Rico, K. I., Sheldon, N. D., Gallagher, T. M., & Chappaz, A. (2019). Redox chemistry and molybdenum burial in a Mesoproterozoic Lake. *Geophysical Research Letters*, 46, 5871–5878. <https://doi.org/10.1029/2019GL083316>

Rico, K. I., Sheldon, N. D., & Kinsman-Costello, L. E. (2020). Associations between redox-sensitive trace metals and microbial communities in a Proterozoic ocean analogue. *Geobiology*, 18, 462–475. <https://doi.org/10.1111/gbi.12388>

Riding, R. (2006). Microbial carbonate abundance compared with fluctuations in metazoan diversity over geological time. *Sedimentary Geology*, 185, 229–238. <https://doi.org/10.1016/j.sedgeo.2005.12.015>

Round, F. E., & Palmer, J. D. (1966). Persistent, vertical-migration rhythms in benthic microflora.: II. Field and laboratory studies on diatoms from the banks of the River Avon. *Journal of the Marine Biological Association of the United Kingdom*, 46, 191–214. <https://doi.org/10.1017/S0025315400017641>

Ruberg, S. A., Kendall, S. T., Biddanda, B. A., Black, T., Nold, S. C., Lusardi, W. R., Green, R., Casserley, T., Smith, E., Sanders, T. G., Lang, G. A., & Constant, S. A. (2008). Observations of the Middle Island Sinkhole in Lake Huron – A unique hydrogeologic and glacial creation of 400 million years. *Marine Technology Society Journal*, 42, 12–21. <https://doi.org/10.4031/00253208787157633>

Schoonen, M. A. A., & Barnes, H. L. (1991). Reactions forming pyrite and marcasite from solution: I. Nucleation of FeS<sub>2</sub> below 100°. *Geochimica et Cosmochimica Acta*, 55, 1495–1504.

Schwedt, A., Kreutzmann, A. C., Polerecky, L., & Schulz-Vogt, H. N. (2012). Sulfur respiration in a marine chemolithoautotrophic *beggiaatoa* strain. *Frontiers in Microbiology*, 2, 276. <https://doi.org/10.3389/fmicb.2011.00276>

Seitaj, D., Schauer, R., Sulu-Gambari, F., Hidalgo-Martinez, S., Malkin, S. Y., Burdorf, L. D. W., Slomp, C. P., & Meysman, F. J. R. (2015). Cable bacteria generate a firewall against euxinia in seasonally hypoxic basins. *Proceedings of the National Academy of Sciences United States of America*, 112, 13278–13283. <https://doi.org/10.1073/pnas.1510152112>

Sharrar, A. M., Flood, B. E., Bailey, J. V., Jones, D. S., Biddanda, B. A., Ruberg, S. A., Marcus, D. N., & Dick, G. J. (2017). Novel large sulfur bacteria in the metagenomes of groundwater-fed chemosynthetic microbial mats in the Lake Huron Basin. *Frontiers in Microbiology*, 8, 791. <https://doi.org/10.3389/fmicb.2017.00791>

Sim, M. S., Bosak, T., & Ono, S. (2011). Large sulfur isotope fractionation does not require disproportionation. *Science*, 333(6038), 74–77. <https://doi.org/10.1126/science.1205103>

Snider, M. J., Biddanda, B. A., Lindback, M., Grim, S. L., & Dick, G. J. (2017). Versatile photophysiology of compositionally similar cyanobacterial mat communities inhabiting submerged sinkholes of Lake Huron. *Aquatic Microbial Ecology*, 79, 63–78. <https://doi.org/10.3354/ame01813>

Taylor, B. E., Wheeler, M. C., & Nordstrom, D. K. (1984). Isotope composition of sulphate in acid mine drainage as measure of bacterial oxidation. *Nature*, 308, 538–541. <https://doi.org/10.1038/308538a0>

Thiel, J., Byrne, J. M., Kappler, A., Schink, B., & Pester, M. (2019). Pyrite formation from FeS and H<sub>2</sub>S is mediated through microbial redox activity. *Proceedings of the National Academy of Sciences United States of America*, 116, 6897–6902.

Voorhies, A. A., Biddanda, B. A., Kendall, S. T., Jain, S., Marcus, D. N., Nold, S. C., Sheldon, N. D., & Dick, G. J. (2012). Cyanobacterial life at low O<sub>2</sub>: Community genomics and function reveal metabolic versatility and extremely low diversity in a Great Lakes sinkhole mat. *Geobiology*, 10, 250–267. <https://doi.org/10.1111/j.1472-4669.2012.00322.x>

Voorhies, A. A., Eisenlord, S. D., Marcus, D. N., Duhaime, M. B., Biddanda, B. A., Cavalcoli, J. D., & Dick, G. J. (2016). Ecological and genetic interactions between cyanobacteria and viruses in a low-oxygen mat community inferred through metagenomics and metatranscriptomics. *Environmental Microbiology*, 18(2), 358–371. <https://doi.org/10.1111/1462-2920.12756>

Wacey, D., McLoughlin, N., Whitehouse, M. J., & Kilburn, M. R. (2010). Two coexisting sulfur metabolisms in a ca. 3400 Ma sandstone. *Geology*, 38, 1115–1118.

Walter, M. R. (1976). Hot-spring sediments in yellowstone national park. In M. R. Walter (Ed.), *Stromatolites* (pp. 489–498). Elsevier.

Zerkle, A. L., Farquhar, J., Johnston, D. T., Cox, R. P., & Canfield, D. E. (2009). Fractionation of multiple sulfur isotopes during phototrophic oxidation of sulfide and elemental sulfur by a green sulfur bacterium. *Geochimica et Cosmochimica Acta*, 73(2), 291–306. <https://doi.org/10.1016/j.gca.2008.10.027>

Zerkle, A. L., Jones, D. S., Farquhar, J., & Macalady, J. L. (2016). Sulfur isotope values in the sulfidic Frasassi cave system, central Italy: A case study of a chemolithotrophic S-based ecosystem. *Geochimica et Cosmochimica Acta*, 173, 373–386. <https://doi.org/10.1016/j.gca.2015.10.028>

#### SUPPORTING INFORMATION

Additional supporting information may be found online in the Supporting Information section.

**How to cite this article:** Gomes, M. L., Klatt, J. M., Dick, G. J., Grim, S. L., Rico, K. I., Medina, M., Ziebis, W., Kinsman-Costello, L., Sheldon, N. D., & Fike, D. A. (2022). Sedimentary pyrite sulfur isotope compositions preserve signatures of the surface microbial mat environment in sediments underlying low-oxygen cyanobacterial mats. *Geobiology*, 20, 60–78.

<https://doi.org/10.1111/gbi.12466>